



**Repositorio Institucional de la Universidad Autónoma de Madrid**  
<https://repositorio.uam.es>

Esta es la **versión de autor** del artículo publicado en:  
This is an **author produced version** of a paper published in:

Advanced Materials 31.39 (2019): 1902582

**DOI:** <https://doi.org/10.1002/adma.201902582>

**Copyright:** © 2019 WILEY-VCH Verlag GmbH & Co. KGaA, Weinheim

El acceso a la versión del editor puede requerir la suscripción del recurso  
Access to the published version may require subscription

## Phthalocyanine-Virus Nanofibers as Heterogeneous Catalysts for Continuous-Flow Photooxidation Processes

*Eduardo Anaya-Plaza, Ana Aljarilla, Grégory Beaune, Nonappa, Jaakko V. I. Timonen, Andrés de la Escosura, Tomás Torres,\* Mauri A. Kostiainen.\**

Dr. Eduardo Anaya-Plaza, Dr. Nonappa, and Prof. Mauri A. Kostiainen  
Department of Bioproducts and Biosystems, Aalto University, Kemistintie 1, 02150 Espoo, Finland.  
E-mail: mauri.kostiainen@aalto.fi

Dr. Ana Aljarilla,<sup>a</sup> Dr. Andrés de la Escosura,<sup>a,b</sup> and Prof. Tomás Torres<sup>a,b,c</sup>  
a) Department of Organic Chemistry, Universidad Autónoma de Madrid (UAM), Calle Francisco Tomás y Valiente, 7, 28049 Madrid, Spain  
b) Institute for Advanced Research in Chemical Sciences (IAdChem), UAM, Campus de Cantoblanco 28049, Madrid, Spain  
c) IMDEA-Nanociencia, Campus de Cantoblanco, 28049 Madrid, Spain  
E-mail: tomas.torres@uam.es

Dr. Grégory Beaune, Dr. Nonappa and Prof. Jaakko V. I. Timonen  
Department of Applied Physics, Aalto University School of Science, Puumiehenkuja 2, FI-02150, Espoo, Finland

**Keywords:** phthalocyanines, reactive oxygen species, viral capsids, self-assembly, heterogeneous catalysis

The generation of highly reactive oxygen species (ROS) at room temperature for application in organic synthesis and wastewater treatment is a great challenge of the current chemical industry. The available options rely mostly on inorganic composites containing toxic heavy metals. The development of biodegradable scaffolds to support ROS generating active sites is an important prerequisite for the production of environmentally benign catalysts. Herein, the electrostatic cocrystallization of a cationic phthalocyanine (Pc) and negatively charged tobacco mosaic virus (TMV) is described, together with the capacity of the resulting crystals to photogenerate ROS. To this end, a novel peripherally-crowded zinc Pc (**1**) was designed and synthesized. With 16 positive charges, this photosensitizer shows no aggregation even in buffer, and is able to act as a molecular glue in the unidimensional assembly of TMV. A step-

wise decrease of ionic strength in mixtures of both components results in exceptionally long fibers, constituted by hexagonally bundled viruses thoroughly characterized by electron and confocal microscopy. The fibers are able to produce ROS in a proof-of-concept microfluidic device, where they were immobilized and irradiated in several cycles, showing a resilient performance. Our bottom-up approach also enables the light-triggered disassembly of fibers after use. This work represents an important example of a biohybrid material with projected application in light-mediated heterogeneous catalysis.

Visible-light mediated oxidation is a fast-developing field with applications in organic synthesis<sup>[1]</sup> and waste water treatment.<sup>[2,3]</sup> In particular, molecular oxygen as oxidation source has gained focused attention, as it is considered as an environmental-friendly approach.<sup>[4]</sup> In this direction, organic chromophores such as porphyrinoids have been employed to convert non-reactive O<sub>2</sub> into reactive oxygen species (ROS) at room temperature, with wide application in nanomedicine<sup>[5,6]</sup> and catalysis.<sup>[7]</sup> Dye-containing heterogeneous catalysts can be easily separated from the reaction medium, offering advantages for scale-up and continuous-flow processes. Highly-ordered structures, such as metal-organic frameworks, have been exploited in this direction as scaffolds to support photoactive molecules in a biomimetic approach.<sup>[7,8]</sup> However, even if the photo-oxidation process itself is as environmentally friendly as possible, a major drawback of these catalysts active sites or structural scaffolds rely on heavy metal atoms.<sup>[9–11]</sup> These undesirable components represent an environmental hazard and, therefore, development of biodegradable supported catalysts is of paramount importance.

Proteins are one of the most functional and versatile biomacromolecules employed by Nature in molecular recognition, transport and catalysis. Creating highly ordered structures *via*

bottom-up assembly of proteins and designed synthetic materials, can lead to fascinating functional biohybrids that combine the best features of biological and synthetic matter.<sup>[12,13]</sup> Among all the chemical assembly strategies employed,<sup>[14,15]</sup> electrostatic interactions present important advantages. For example, they enable the use of native proteins without genetic or chemical modification and offer the possibility to design multi-stimuli assembly/disassembly processes, capital in the design of responsive materials.<sup>[16,17]</sup> The role that shape,<sup>[18]</sup> electrostatic potential<sup>[19–21]</sup> and specific nearest neighbor interactions of the protein scaffold plays in the crystallization process is well established.<sup>[22,23]</sup> Importantly, strategies to control the interaction between the protein and the co-crystallization agent by means of pH and ionic strength of the aqueous media has enabled fine tuning in the kinetics of the assembly process, leading to high structural control. Recent examples of protein crystal scaffolds with catalytic activity indicate that biohybrids can function as efficient catalysts.<sup>[24–27]</sup> While protein cages such as (apo)ferritin or cowpea chlorotic mottle virus have coped the most recent developments in three-dimensional electrostatic assemblies, other protein scaffolds such as tobacco mosaic virus (TMV) have been recently explored, yielding unidimensional morphologies.<sup>[28]</sup>

Among the porphyrinoids available, phthalocyanines (Pc) hold a prominent place due to their outstanding optical properties.<sup>[29–31]</sup> These non-natural photosensitizers consist of four isoindole units linked through nitrogen atoms, which are extendedly conjugated and yield intense absorption in the red/ near-infrared region of the visible spectrum. In particular, zinc derivatives (ZnPc) present a characteristic sharp absorption band between 670–700 nm, as well as moderate to high fluorescence quantum yields. Furthermore, ZnPc are reported to produce ROS, a compendium of highly reactive oxidation agents such as superoxide, peroxides and singlet oxygen, which can be utilized in photodynamic therapy, diagnostic

arrays and catalysis. We have previously reported spherical protein cage-Pc co-crystal with maintained light-induced excited state properties.<sup>[32]</sup> Herein, we report the enhanced properties arising from the co-crystallization between rod-like TMV and a highly charged ZnPc *via* electrostatic interactions into highly ordered fibers. Immobilization of the dye in fibers, in comparison with the dye free in solution, yields a heterogeneous catalyst allowing rapid purification by physical methods. Additionally, the high-aspect ratio of the fibers gives a high contact area with the media. On the other hand, the use of responsive self-assembled biohybrids, allow us to dispose of them with the adequate stimuli, yielding exclusively biodegradable material. Such assemblies can be used as aqueous media oxidizing agents with potential application in green organic chemistry and water treatment.

The use of Pc in aqueous media is associated with several challenges, such as lack of solubility, high hydrophobicity and aggregation, compromising their performance. In order to circumvent these issues we have designed and synthesized a novel ZnPc bearing eight 2,6-bis-(3-methylpyridinium)phenoxy moieties (**1**) at the  $\beta$  position of the isoindole units (**Figure 1a**). The challenging synthesis of this unique chromophore was accomplished in four main steps (Scheme S1). Briefly, 2-benzyloxy-1,3-dibromobenzene was coupled with pyridin-3-ylboronic acid *via* Suzuki-Miyaura reaction which, after deprotection, yielded 2,6-bis(pyridine-3-yl)phenol. Second, nucleophilic aromatic substitution of 4,5-dichlorophthalonitrile with the previously synthesized phenol led to the desired disubstituted phthalonitrile exclusively under highly energetic microwave radiation. Otherwise, thermal reaction in the same conditions yielded the monosubstituted derivative due to the high steric hindrance of the nucleophilic groups. The third step consisted on the cyclotetramerization of the described phthalonitrile in the presence of Zn(OAc)<sub>2</sub>, resulting into the precursor phthalocyanine bearing 16 pyridine groups (compound **8** in the SI). Last, permethylation of **8**

in presence of methyl iodide resulted in the water soluble ZnPc **1**. The substitution pattern in this molecule renders a unique photosensitizer with enhanced performance in aqueous media. Peripheral decoration directs the 16 positively charged moieties out of the ZnPc plane (**Figure 1b**), hindering the typical columnar aggregation through  $\pi$ - $\pi$  stacking in aqueous environment, which is known to quench excited-state properties such as fluorescence and ROS production. This was clearly shown by the sharp absorption band observed in a broad range of salt concentrations (**Figure 1c**), as well as maintained emission when excited at 615 nm (**Figure 1d**). On the other hand, other water soluble ZnPc bearing 8 N-methylpyridinium moieties (compound **9** in the SI) presented a strong aggregation by increasing NaCl concentration, as shown by the band shift from 675 to 635 nm as well as a complete emission quench (Figure S1).

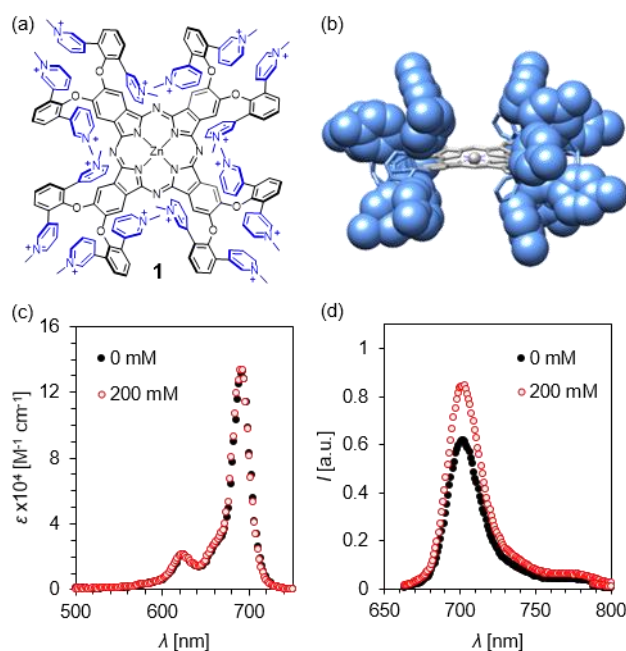


**Figure 1.** (a) Chemical structure of ZnPc **1**. Iodide counterions are omitted for clarity. (b) 3D structure obtained by *ab initio* calculations at semi-empirical level (PM3). Pyridinium moieties shown as spheres. Absorption (c) and emission (d) spectra of **1** at 0 and 200 mM of NaCl.

TMV is a helical array of 2130 coat proteins of an approximate weight of 17 kDa, wrapping the viral RNA. This results in a 300 nm long, 18 nm diameter rod-like virus with an estimate molecular weight of 39400 kDa (**Figure 2a-b**). This geometry, which renders a negatively charged helix on the outer surface of the virus at pH above 4.5,<sup>[33]</sup> can function as a well-defined scaffold for unidimensional ensembles. TMV has been employed as drug delivery platform,<sup>[34–36]</sup> as well as building block in different biohybrid arrays together with small functional molecules,<sup>[37]</sup> or nanoparticles.<sup>[28,38,39]</sup>

In order to understand how **1** and TMV interact, the saturation ratio (i.e. full coverage of TMV by photosensitizers) between **1** and TMV was determined by dynamic light scattering (DLS). TMV concentration was fixed at 0.1 mg mL<sup>-1</sup> and, assuming a molecular weight of 39.8 MDa, increasing ratios between 0 and 25000 equivalents of **1** were added. We observed the decrease of the peak at 300 nm, which corresponds to the unimeric TMV, while a new peak above 2000 nm arises, which corresponds to aggregated TMV (**Figure 2c**). Monitoring the derived count rate we found the initial increase of the signal above 1000 equivalents, establishing the starting point of assembly, while the saturation point was reached above 15000 equivalents (**Figure 2d**). However, previously reported assembly of TMV shows concentration dependence.<sup>[40,41]</sup> In fact, when the concentration of the virus has risen to 10 mg/mL, saturation of the virus is reached above 10000 equivalents, as we observe the precipitate formation, while a deep-colored supernatant remains. Therefore, unless stated otherwise, a ratio of 10000 was employed in the following experiments.

Electrostatically assembled protein crystals are highly dependent on the ionic strength of the media. Therefore, preparation of high aspect-ratio fibers was achieved by step-wise decrease of the NaCl concentration in the media (**Figure 2e**). TMV and **1** were mixed in acetate buffer 10 mM pH 5.5 containing 150 mM of NaCl and no complex formation was observed. The

solution was dialyzed against the same buffer containing 125, 100, 75, 50, 25 and finally 0 mM of NaCl, yielding the aforementioned fibers. This electrostatically driven assembly is fully reversible and the fibers show disassembly upon increasing the ionic strength (Figure S2).

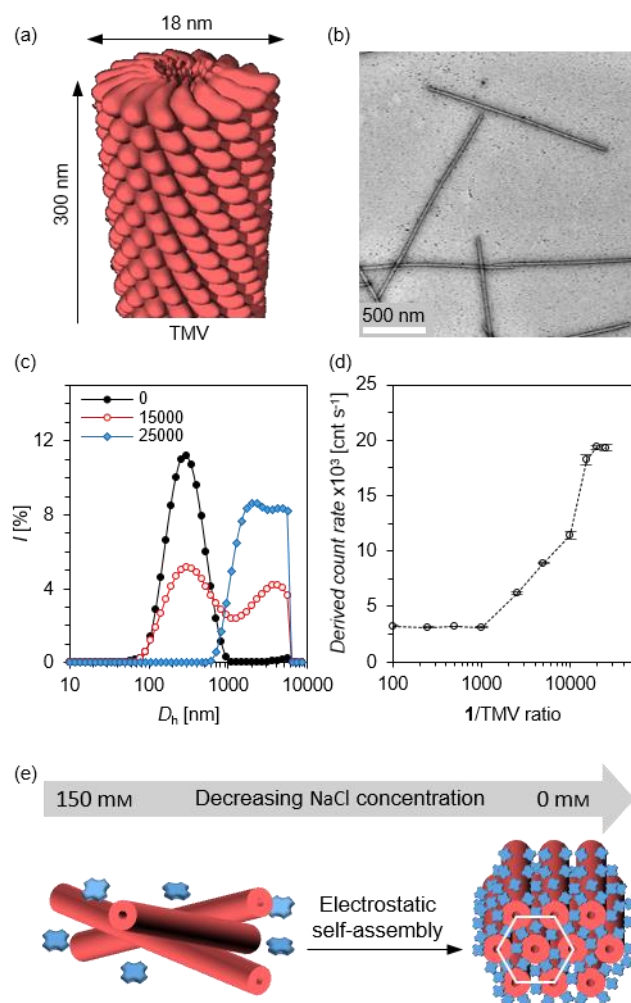


**Figure 2.** (a) Structure model and (b) TEM image of TMV. (c) DLS intensity profiles of TMV (0.1 mg/mL) in presence of 0, 15000 and 25000 equivalents of **1** (black, red and blue dots, respectively). (d) Derived count rate of TMV (0.1 mg/mL) in presence of increasing ratios of **1**, showing saturation above 15000 equivalents. (e) Schematic representation of the step-wise approach to obtain crystalline hybrids, showing no interaction at high ionic strength (150 mM NaCl) and high-ordered materials at low ionic strength (0 mM NaCl).

The resulting complexes were structurally characterized by different techniques (**Figure 3**).

Optical microscopy images show the fibrous morphology of the bundles, with thread lengths



in the hundreds of  $\mu\text{m}$  and thicknesses between 1–2  $\mu\text{m}$  (**Figure 3a**). Taking into account the TMV dimensions ( $300 \times 18 \text{ nm}$ ), this morphology is the consequence of a spontaneous highly directional assembly process, where TMV acts as self-assembling building block, providing a protein-based scaffold that supports the photosensitizer. Small angle X-ray scattering (SAXS, **Figure 3b**) measurements reveal that the fibers present two-dimensional (2D) hexagonal packing perpendicular to the fiber vector. Three main diffraction peaks ( $q = 0.0354, 0.0632, 0.0727 \text{ \AA}^{-1}$ ) were found, which correspond to the reflections from (10), (11) and (20) planes respectively. Linear fitting of the squared diffraction peak indices as a function of the measured  $q$ -values yields a lattice constant of  $a = 20.1 \text{ nm}$  (**Figure 3c**). This is in good agreement with the typical packaging of highly concentrated TMV,<sup>[42]</sup> or in presence of atomic cations<sup>[41,43]</sup> or small-size AuNPs.<sup>[28]</sup> The observed lattice parameter is slightly higher than the TMV diameter (*i.e.* 18 nm), which is in close agreement with the proposed model. On the other hand, direct combination of **1** and TMV capsids in acetate buffer 10 mM pH 5.5 in the absence of NaCl results in the immediate sedimentation of a green-colored fibrous complexes. Observed under the optical microscope, the fibers are shorter and thicker (Figure S3). These quickly assembled fibbers do not show any scattering peaks in SAXS analysis because of their amorphous structure.

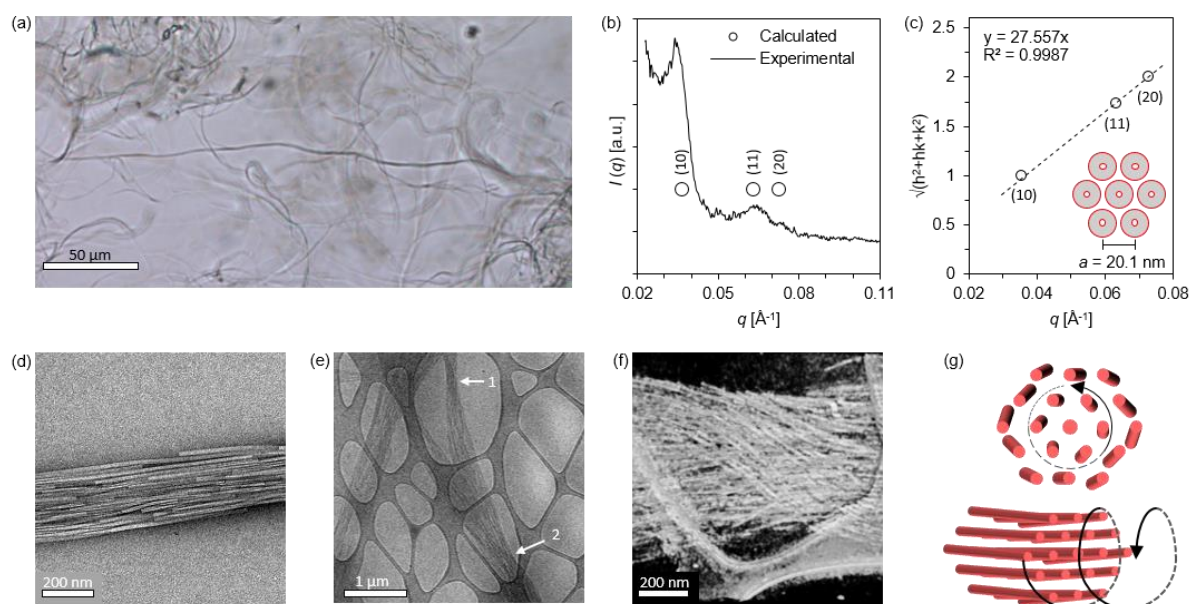


**Figure 3.** Structural characterization of the **1**-TMV fibers. (a) Optical micrograph showing the fibers and their entanglement. (b) SAXS measured (line) of the hybrids. The simulated data (dots) were calculated assuming  $a = 20.1$  nm. (c) The squared diffraction peak indices plotted as a function of the measured  $q$ -values. A linear fit yields  $a = 18.5$  nm for a 2D hexagonal lattice. (d) TEM image showing the **1**-TMV fibers and their fine structure (e), constituted by parallel alignment of individual TMV capsids. (f) cryo-EM image of the biohybrids, showing features of their higher order organization in twists (1) and bundles (2) to form bigger fibers. (g) A cryo-ET density map of a twist, showing right-handed helicity.

Further structural insight of the highly ordered fibers was obtained by ambient- and cryo-electron microscopy (**Figure 3d-f**). High-magnification images of the fibers confirm the parallel alignment and side-by-side packing of the individual viruses. No periodic order along the fiber axis was observed, which supports the 2D structure obtained by SAXS. Additionally, cryo-TEM images show similar features as observed in the macro scale, such as twists and bifurcations (**Figure 3f**). The helical twists were 3D reconstructed, showing a transfer of the chirality from the individual virus to the bundle. As shown in **Figure 3g**, right-handed helicity was found, which is in good agreement with previously reported TMV bundles.

As a consequence of the anisotropy inherent to one-dimension ordered materials, the fibers present birefringence of polarized light (**Figure 4a**). They show strong blue color when

oriented 45° respect the cross-polarizers, in opposition to other possible orientations (Figure S4). Otherwise, the interaction with the virus does not affect the optical properties of **1**, as shown by the sharp absorption of the hybrid at 692 nm (**Figure 4b**). This confirms the unaltered excited state properties of **1** even when packed with TMV. In fact, strong fluorescence of the fibers can be observed when irradiated at 633 nm. This property opens up new characterization possibilities like confocal microscopy, which offers better resolution than optical microscopy. Hybrids shown in **Figure 4c** were characterized with this technique and the images reinforce the hypothesis of the hierarchical fiber ensemble of smaller threads.

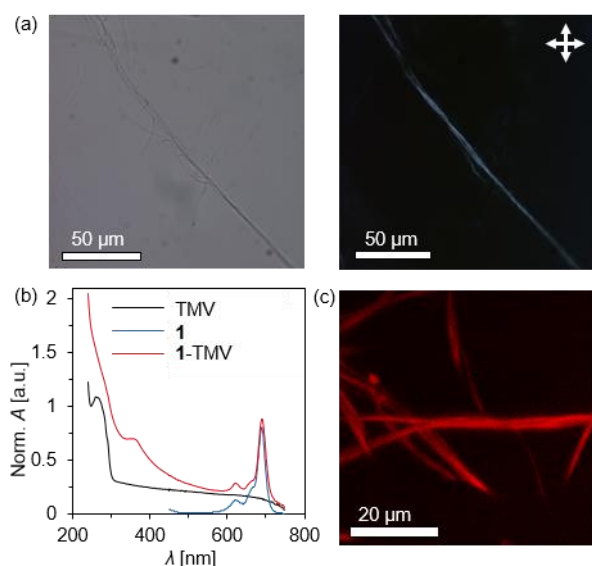


**Figure 4.** (a) Optical (left) and polarized light (right) microscopy images. The latter was taken between cross-polarizers, aligned as shown in top-right corner vectors. (b) Normalized absorption spectra of the **1**-TMV hybrid (red), compared to the TMV (black) and **1** (blue) in acetate buffer (10 mM pH = 5.5). (c) Confocal microscopy image of the hybrids ( $\lambda_{\text{exc}} = 633$  nm).

Utilizing compound **1** as a molecular glue in the aforementioned biohybrids present several advantages, such as high solvent-accessible surface, which yields an ideal platform for heterogeneous photooxidation. In our approach, we hypothesize that **1** maintains its ROS generation ability despite the fact that it is immobilized within the biohybrid. In order to

demonstrate this, ROS photogeneration was monitored by the well-known fluorescence indicator 2',7'-dichlorodihydrofluorescein ( $\text{H}_2\text{DCF}$ ) which oxidizes in presence of ROS to highly fluorescent 2',7'-dichlorofluorescein (DCF, **Figure 5a**). The fibers were placed on a glass slide, covered with  $750\ \mu\text{M}$   $\text{H}_2\text{DCF}$  and then irradiated by excitation at 488 (green) and 633 nm (red). The former excites the sensor, while the latter excites the **1**-TMV fibers. Images were taken in a continuous way (each being the average of 4 images, 1.96 s per frame). We observed the DCF intensity increasing over the time exclusively in the near proximity of the fiber bundles (**Figure 5b**), as a consequence of the ROS photogeneration. On the other hand, areas without fibers present no emission in neither wavelength, serving as a negative control. Photooxidation dependence on molecular oxygen present in the media, as well as the ZnPc was demonstrated in control experiments (Figure S5 and S6).

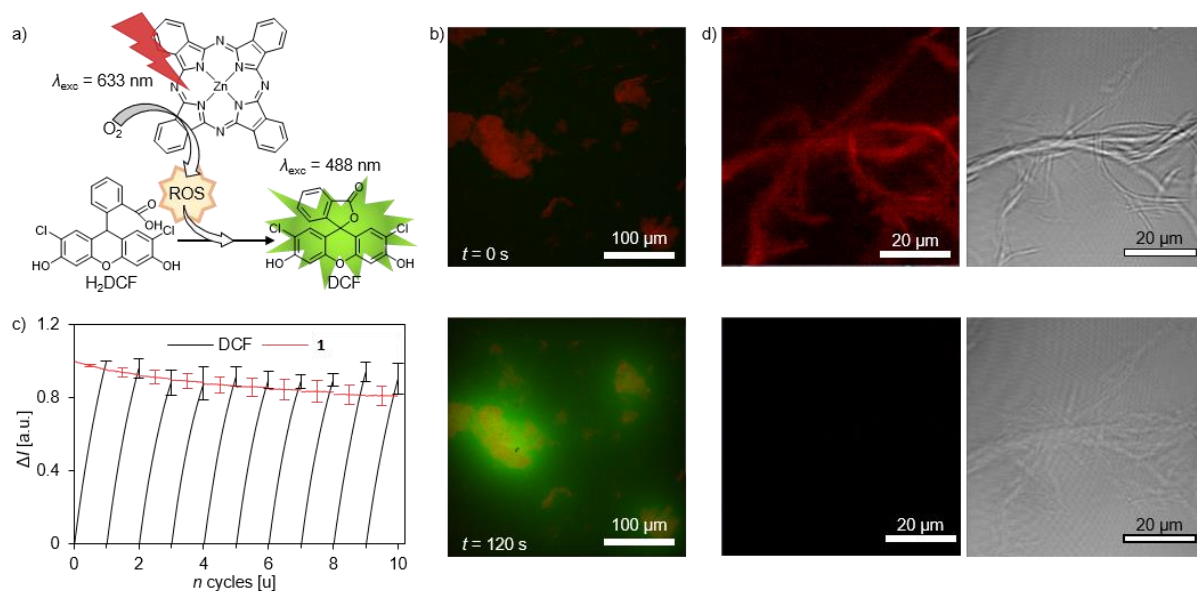


**Figure 5.** (a) Schematic representation of the photoinduced oxidation process. Absorption of red light ( $\lambda_{\text{exc}} = 633\text{ nm}$ ) by the chromophore induces the excitation of molecular oxygen present in the media to ROS, which oxidizes the precursor ( $\text{H}_2\text{DCF}$ , non-fluorescent) into DCF ( $\lambda_{\text{exc}} = 488\text{ nm}$ ). Note that the peripheral substituents of **1** has been omitted for clarity purposes. (b) Time-lapsed emission microscopy images of the bundled fibers (red) and *in-situ* photooxidized DCF (green).  $\text{H}_2\text{DCF}$  is present at  $750\ \mu\text{M}$  in acetate buffer (10 mM pH = 5.5).

(c) Averaged and normalized increase of DCF (black) and decrease of **1** (red) after 2 min irradiation (60 frames) per cycle. Error bars correspond to the standard deviation of three bundles. Normalized data to the end value of the first cycle (DCF) and the initial emission **1**. (d) Emission (*left*) and bright field (*right*) micrographs of fibers before (*top*) and after (*bottom*) intense irradiation, showing the photobleaching of the ZnPc and, as consequence, loss of their structural stability.

One challenge of photochemical oxidation in aqueous media is to transfer this potential into continuous flow set-ups. However, our fiber-like morphology allowed to immobilize the bundles inside a proof-of-concept device (Figure S7) consisting of a rectangular cross-section capillary (0.2 x 2.0 x 50 mm). The capillary was fed with H<sub>2</sub>DCF 750  $\mu$ M in acetate buffer (10 mM pH = 5.5), in order to maintain the conditions as close as possible to the formation of the fibers. Controlling the inlet flow and irradiation conditions allowed us to test the reproducibility of the ROS photogeneration and stability of the fibers under irradiation. In this setup, previously described irradiation conditions were employed, obtaining similar results after 2 minutes of continuous irradiation. Fluorescence intensity of DCF (green channel) was measured as the average of three circular ROI within the bundle and corrected with the average of three circular ROI far from the bundle, which serves as background signal. In a similar way, emission intensity of **1** was measured employing the same ROI in order to measure the fiber photostability. Subsequent washing with fresh H<sub>2</sub>DCF solution (c.a. 6  $\mu$ L s<sup>-1</sup> over 15 s) washed-out the remaining DCF without detaching the fibers, allowing us to repeat over 10 cycles. The average obtained from three bundles was plotted (**Figure 5c**). First, we observed remarkable stability of the fibers to the process: red intensity decreases just above 10 % after 10 cycles (20 min of continuous irradiation). Additionally, no important intensity loss is observed between cycles, which support the effective immobilization of the fibers into the channel. Secondly, ROS production is consistent and stable, with a slight decrease in the final intensity due to the slight loss of photosensitizer.

One of the main advantages of supramolecularly assembled materials is their ability to disassemble under given stimuli. In our case, there is an opportunity to dispose the active material once the desired photooxidation has been achieved. To this end, the fibbers were irradiated with laser intensities 20 times higher than the one used in the previous experiment. After a few seconds of irradiation, we observed a fast decrease in the emission as a consequence of the photobleaching of **1**, which triggers the dissolution of the samples as shown in the bright field images (**Figure 5d**). This results in a green solution to the disposal of the active materials, in opposition to the non-soluble inorganic materials typically used in catalysis.

In conclusion, we have designed, synthesized and characterized a new biohybrid material obtained by the electrostatic interaction between the TMV capsid and a specifically designed ZnPc, yielding a unique morphology with optical activity. The chromophore presents 16 positive charges and resilient optical properties in aqueous media of varying ionic strengths. The cationic chromophore can act as molecular glue and direct the assembly of the rod-like viruses into hexagonally packed fibers. Additionally to their interesting structural features, the resulting high aspect-ratio fibers maintain the optical properties of the dye, namely fluorescence and singlet oxygen production. The first one allowed us to characterize the fibers by confocal microscopy. The second enabled us to demonstrate that the fibers are easily immobilized in capillaries, while their singlet oxygen production remains stable after several oxidation/flushing cycles. In addition, our self-assembly approach offers the possibility to disassembly the fibers by laser irradiation. This work represent a new approach to tackle continuous-flow photooxidations processes in aqueous media.

### Supporting Information

Supporting Information is available from the Wiley Online Library or from the author.

### Acknowledgements

EA-P acknowledges the funding from the European Union's Horizon 2020 research and innovation programme under the Marie Skłodowska-Curie grant agreement No 794536 (BiHyOMat). AdIE received support from the Spanish Ministry of Economy and Competitiveness (MINECO: CTQ-2017-89539-P and EUIN2017-87022). TT acknowledges the financial support from Spanish MINECO [CTQ2017-85393-P and PCIN-2017-042/EuroNanoMed2017-191, TEMPEAT]. JVIT was supported by funding from Academy of Finland and ERC. MAK was supported by the Academy of Finland (Grants 308578, 303804) and Sigrid Juselius Foundation are gratefully acknowledged. This work was carried out under the Academy of Finland's Centers of Excellence Programme and made use of the Aalto University Nanomicroscopy Centre (Aalto NMC).

Received: ((will be filled in by the editorial staff))

Revised: ((will be filled in by the editorial staff))

Published online: ((will be filled in by the editorial staff))

- [1] C. Bian, A. K. Singh, L. Niu, H. Yi, A. Lei, *Asian Journal of Organic Chemistry* **2017**, 6, 386.
- [2] R. Ma, S. Zhang, T. Wen, P. Gu, L. Li, G. Zhao, F. Niu, Q. Huang, Z. Tang, X. Wang, *Catalysis Today* **2018**, S0920586118315189.
- [3] J. Herney-Ramirez, M. A. Vicente, L. M. Madeira, *Applied Catalysis B: Environmental* **2010**, 98, 10.
- [4] S. Fukuzumi, Y.-M. Lee, J. Jung, W. Nam, *Green Chemistry* **2018**, 20, 948.
- [5] V. Almeida-Marrero, E. van de Winckel, E. Anaya-Plaza, T. Torres, A. de la Escosura, *Chemical Society Reviews* **2018**, 47, 7369.
- [6] S. Singh, A. Aggarwal, N. V. S. D. K. Bhupathiraju, G. Arianna, K. Tiwari, C. M. Drain, *Chemical Reviews* **2015**, 115, 10261.
- [7] M. Zhao, S. Ou, C.-D. Wu, *Accounts of Chemical Research* **2014**, 47, 1199.
- [8] J. Chakraborty, I. Nath, F. Verpoort, *Coordination Chemistry Reviews* **2016**, 326, 135.
- [9] Z. Lin, Z.-M. Zhang, Y.-S. Chen, W. Lin, *Angewandte Chemie International Edition* **2016**, 55, 13739.
- [10] C. Pereira, M. Simões, J. Tomé, F. Almeida Paz, *Molecules* **2016**, 21, 1348.
- [11] F. Scandola, C. Chiorboli, A. Prodi, E. Iengo, E. Alessio, *Coordination Chemistry Reviews* **2006**, 250, 1471.

- [12] B. J. G. E. Pieters, M. B. van Eldijk, R. J. M. Nolte, J. Mecinović, *Chemical Society Reviews* **2016**, *45*, 24.
- [13] S. Abe, B. Maity, T. Ueno, *Chemical Communications* **2016**, *52*, 6496.
- [14] Y. Bai, Q. Luo, J. Liu, *Chemical Society Reviews* **2016**, *45*, 2756.
- [15] Q. Luo, C. Hou, Y. Bai, R. Wang, J. Liu, *Chemical Reviews* **2016**, *116*, 13571.
- [16] M. A. Kostianen, O. Kasyutich, J. J. L. M. Cornelissen, R. J. M. Nolte, *Nature Chemistry* **2010**, *2*, 394.
- [17] V. Liljeström, J. Mikkilä, M. A. Kostianen, *Nature Communications* **2014**, *5*, 4445.
- [18] Y. Wang, Y. Wang, D. R. Breed, V. N. Manoharan, L. Feng, A. D. Hollingsworth, M. Weck, D. J. Pine, *Nature* **2012**, *491*, 51.
- [19] A. M. Kalsin, M. Fialkowski, M. Paszewski, S. K. Smoukov, K. J. M. Bishop, B. A. Grzybowski, *Science* **2006**, *312*, 420.
- [20] M. A. Kostianen, P. Hiekkataipale, A. Laiho, V. Lemieux, J. Seitsonen, J. Ruokolainen, P. Ceci, *Nature Nanotechnology* **2013**, *8*, 52.
- [21] A. H. Gröschel, A. Walther, T. I. Löblich, F. H. Schacher, H. Schmalz, A. H. E. Müller, *Nature* **2013**, *503*, 247.
- [22] D. Nykypanchuk, M. M. Maye, D. van der Lelie, O. Gang, *Nature* **2008**, *451*, 549.
- [23] S. Y. Park, A. K. R. Lytton-Jean, B. Lee, S. Weigand, G. C. Schatz, C. A. Mirkin, *Nature* **2008**, *451*, 553.
- [24] M. Lach, M. Künzle, T. Beck, *Chemistry - A European Journal* **2017**, *23*, 17482.
- [25] M. Künzle, T. Eckert, T. Beck, *Journal of the American Chemical Society* **2016**, *138*, 12731.
- [26] M. Uchida, K. McCoy, M. Fukuto, L. Yang, H. Yoshimura, H. M. Miettinen, B. LaFrance, D. P. Patterson, B. Schwarz, J. A. Karty, P. E. Prevelige, B. Lee, T. Douglas, *ACS Nano* **2018**, *12*, 942.
- [27] N. K. Beyeh, Nonappa, V. Liljeström, J. Mikkilä, A. Korpi, D. Bochicchio, G. M. Pavan, O. Ikkala, R. H. A. Ras, M. A. Kostianen, *ACS Nano* **2018**, *12*, 8029.
- [28] V. Liljeström, A. Ora, J. Hassinen, H. T. Rekola, Nonappa, M. Heilala, V. Hynninen, J. J. Joensuu, R. H. A. Ras, P. Törmä, O. Ikkala, M. A. Kostianen, *Nature Communications* **2017**, *8*, 671.
- [29] H. Lu, N. Kobayashi, *Chemical Reviews* **2016**, *116*, 6184.
- [30] A. B. Sorokin, *Chemical Reviews* **2013**, *113*, 8152.
- [31] R. C. H. Wong, P.-C. Lo, D. K. P. Ng, *Coordination Chemistry Reviews* **2019**, *379*, 30.
- [32] J. Mikkilä, E. Anaya-Plaza, V. Liljeström, J. R. Caston, T. Torres, A. de la Escosura, M. A. Kostianen, *ACS Nano* **2016**, *10*, 1565.
- [33] M. Bendahmane, M. Koo, E. Karrer, R. N. Beachy, *Journal of Molecular Biology* **1999**, *290*, 9.
- [34] A. E. Czapar, Y.-R. Zheng, I. A. Riddell, S. Shukla, S. G. Awuah, S. J. Lippard, N. F. Steinmetz, *ACS Nano* **2016**, *10*, 4119.
- [35] A. A. Vernekar, G. Berger, A. E. Czapar, F. A. Veliz, D. I. Wang, N. F. Steinmetz, S. J. Lippard, *Journal of the American Chemical Society* **2018**, *140*, 4279.
- [36] P. L. Chariou, L. Wang, C. Desai, J. Park, L. K. Robbins, H. A. Recum, R. A. Ghiladi, N. F. Steinmetz, *Macromolecular Bioscience* **2019**, 1800407.
- [37] Y. Tian, X. Yan, M. L. Saha, Z. Niu, P. J. Stang, *Journal of the American Chemical Society* **2016**, *138*, 12033.
- [38] E. Dujardin, C. Peet, G. Stubbs, J. N. Culver, S. Mann, *Nano Letters* **2003**, *3*, 413.



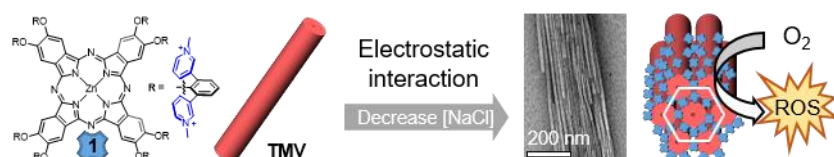
- [39] T. Nakajima, K. Sano, M. Mitsunaga, P. L. Choyke, H. Kobayashi, *Cancer Research* **2012**, 72, 4622.
- [40] A. Nedoluzhko, T. Douglas, *Journal of Inorganic Biochemistry* **2001**, 84, 233.
- [41] T. Li, R. E. Winans, B. Lee, *Langmuir* **2011**, 27, 10929.
- [42] T. Li, X. Zan, R. E. Winans, Q. Wang, B. Lee, *Angewandte Chemie International Edition* **2013**, 52, 6638.
- [43] L. Yang, S. Wang, M. Fukuto, A. Checco, Z. Niu, Q. Wang, *Soft Matter* **2009**, 5, 4951.

Light-mediated oxidation in heterogeneous catalysis represent a desirable goal for several technologies. Herein, we present the synthesis of a sterically hindered phthalocyanine with maintained properties in aqueous media. This photosensitizer triggers the assembly into hexagonal lattices of *tobacco mosaic virus* that resulted into high aspect-ratio fibers with reactive oxygen species generation. The applicability of the fibers as heterogeneous catalysts is demonstrated in a proof-of-concept device.

**Keyword** phthalocyanines, reactive oxygen species, viral capsids, self-assembly, heterogeneous catalysis

Eduardo Anaya-Plaza, Ana Aljarilla, Grégory Beaune, Nonappa, Jaakko V. I. Timonen, Andrés de la Escosura, Tomás Torres,\* Mauri A. Kostianen.\*

### Phthalocyanine-Virus Nanofibers as Heterogeneous Catalysts for Continuous-Flow Photooxidation Processes



## Supporting Information

### **Phthalocyanine-Virus Nanofibers as Heterogeneous Catalysts for Continuous-Flow Photooxidation Processes**

*Eduardo Anaya-Plaza, Ana Aljarilla, Grégory Beaune, Nonappa, Jaakko V. I. Timonen, Andrés de la Escosura, Tomás Torres, Mauri A. Kostianen.*

1. Chemicals and instruments.....	S2
2. Synthesis of <b>1</b> .....	S5
3. Aggregation in NaCl concentrations .....	S9
4. Fibers dissociation.....	S10
5. <b>1</b> -TMV conjugates .....	S11
6. Angle variation under cross polarizers.....	S11
7. ROS controls .....	S12
8. Oxygen dependence .....	S13
9. Proof-of-concept device .....	S14
10. Characterization spectra .....	S15
11. Bibliography.....	S39

## 1. Chemicals and instruments

*Synthesis – General Considerations:* All reagents were used as purchased from commercial sources (Sigma Aldrich) without further purification. Solvents were purchased from Carlo Erba Reagents and dried through standard techniques prior to use. Dialysis membrane (Spectra/Por® Biotech CE tubing MWCO: 100-500 D) was purchased from Spectrum Laboratories, Inc. All reactions were performed in standard glassware, under inert argon atmosphere when indicated. Microwave reactions were carried out in a CEM Discovery monomode reactor. Reactions were monitored by thin-layer chromatography (TLC) using TLC plates precoated with silica gel 60F254 (Merck). Column chromatography was carried out on Merck's silica gel 60, 40–63  $\mu\text{m}$  (230–400 mesh).  $^1\text{H}$  and  $^{13}\text{C}$  NMR spectra were recorded using Bruker AC-300 (300 MHz) instruments, and the solvent signal was used for internal calibration. UV–Vis spectra were recorded with Cytation 3 cell imaging multi-mode reader from BioTek Instruments. Fluorescence spectroscopy was recorded with QuantaMaster 40 from Photon Technology. Matrix-assisted laser desorption/ionization - time of flight (MALDI-TOF) and electrospray ionization (ESI) mass spectra were recorded with a Bruker Ultrareflex III spectrometer and with an Applied Biosystems QSTAR using an injection system HPLC1100 (Agilent Technologies), respectively.

*Fiber preparations:* In an Eppendorf tube, 20  $\mu\text{L}$  of a TMV solution (10  $\text{mg mL}^{-1}$ ) in acetate buffer (10 mM, pH 5.5) was subsequently mixed with 8.5  $\mu\text{L}$  of acetate buffer (10 mM, pH 5.5), 1.5  $\mu\text{L}$  of NaCl 5 M, and 20  $\mu\text{L}$  of **1** (2.5 mM). Under this conditions (150 mM of NaCl), no fiber precipitation was observed. This solution was dialyzed (100-500 MWCO) against 200 mL of acetate buffer (10 mM, pH 5.5) with decreasing amounts of NaCl (125, 100, 75, 50, 25 and 0 mM) for 45 min each step, followed by overnight dialysis against 0 mM NaCl. Fibers were collected afterwards and the fibers were left precipitate during 24h at 4  $^{\circ}\text{C}$ .

*Microscopy equipment:* Optical microscope images of **1**-TMV fibers were taken with a Leica DM4500 microscope equipped with cross-polarizers. Sample (10  $\mu\text{L}$ ) was deposited on a glass slide and covered with a cover slide stick with double-side tape in order to preserve the structural features of the sample.

The fibers and the sensor inside the capillary were imaged and recorded by confocal microscopy (LSM 710, 5X/0.16 water immersion objective;  $\lambda_{\text{ex}1} = 488 \text{ nm}$  and  $\lambda_{\text{em}1} = 498 - 624 \text{ nm}$  for the observation of the sensor;  $\lambda_{\text{ex}2} = 633 \text{ nm}$  and  $\lambda_{\text{em}2} = 635 - 758 \text{ nm}$ ). Images were recorded at an acquisition rate of 1 frame every 1.94 s and were exported from the instrument software (Zeiss Zen Black) in CZI format and further processed with Fiji (version 1.52d).

Microfluidic devices were prepared by UV-curing a rectangular glass capillary (CM Scientific, 0.2 x 2.0 x 50 mm) on a microscopy slide and a needle (25Gx5/8") on one side of the capillary. The needle was then connected to a reservoir through a PTFE tubing (Length = 35 cm, ID = 256  $\mu\text{m}$ ). The reservoir was filled with the sensor at 750  $\mu\text{M}$  in acetate buffer (10 mM, pH 5.5) and connected to a piezoelectric controller unit (Elveflow). The tubing was filled with the sensor, then the fibers were carefully aspirated in the tubing, the tubing was connected to the needle and then the capillary was filled with the sensor and the fibers.

The fibers were irradiated for 2 min and then DCF is washed out with fresh  $\text{H}_2\text{DCF}$  for 15 s with a flow of  $6 \mu\text{L s}^{-1}$ . This cycle is repeated 10 times in a row on 3 different fibers.

*Negative controls:* Concentration of **1** was determined by absorption spectroscopy, and found to be  $\sim 1 \times 10^{-5}$  M (Figure S5a). **1**-TMV shows higher photogeneration than **1** free in solution, due to the heterogeneous distribution of **1** within the fibers, while TMV ( $\sim 1 \text{ mg mL}^{-1}$ ) shows no detectable response. On the other hand, oxygen free sample (Figure S6) was achieved by thorough  $\text{N}_2$  bubbling of DFC solution and the pre-formed fibers (note smaller size of fibers due to mechanical stress), followed by encapsulation of the solution within a glass capillary (see above) in order to prevent ambient oxygen diffusion into the solution.

*Cryogenic Transmission Electron Microscopy (Cryo-TEM):* The cryo-TEM images were collected using JEM 3200FSC field emission microscope (JEOL) operated at 300 kV in bright field mode with Omega-type Zero-loss energy filter. Prior to sample preparation, 200 mesh copper grids with lacey carbon support film (Electron Microscopy Sciences) were plasma cleaned using Gatan Solarus (Model 950) plasma cleaner for 30 seconds. The samples for Cryo-TEM imaging were prepared by placing  $3 \mu\text{L}$  of a freshly prepared aqueous dispersion of the sample on a plasma treated TEM grids and plunge-freezed into  $-170^\circ\text{C}$  ethane/propane mixture using Vitrobot™ 2 s blotting time under 100 % humidity. The vitrified specimen were cryo-transferred to the microscope. The images were acquired with Gatan Digital Micrograph® software while the specimen temperature was maintained at  $-187^\circ\text{C}$ .

*Serial EM and Electron Tomography Reconstruction:* Tilt series of 2D projections were acquired with the SerialEM-software package.<sup>[1]</sup> Specimen was tilted between  $\pm 69^\circ$  angles with  $2\text{--}3^\circ$  increment steps to collect stack files. The original stack files were then subjected for fine alignment and cropping with IMOD.<sup>[2]</sup> The images were binned twice to reduce noise and computation time. Maximum entropy method (MEM).<sup>[3,4]</sup> reconstruction scheme was carried out with custom made program on Mac or Linux cluster with regularization parameter value of  $\lambda=1.0 \text{ e}^{-3}$ . Volumetric graphics and image analyses were performed with the UCSF Chimera package.

*Ambient transmission electron microscopy (TEM):* imaging of TMV particles and **1**-TMV fibers was carried out with Tecnai 12 Bio-Twin electron microscope (JEOL) using an acceleration voltage of 120 kV. Sample ( $3 \mu\text{l}$ ) was added on 200 mesh copper grid with carbon support film (CF-Quantifoil) for one minute and the excess sample was blotted away with filter paper. Uranyl phosphate was used as negative stain.

*Dynamic light scattering:* The hydrodynamic diameter ( $D_H$ ) of the TMV samples ( $0.1 \text{ mg mL}^{-1}$ ) was measured using a standard dynamic light scattering device (Zetasizer Nano Series, Malvern Instruments) with a 4 mW He-Ne ion laser at a wavelength of 633 nm and an avalanche photodiode detector at an angle of  $173^\circ$ . Experiments were carried out at  $25^\circ\text{C}$ . Plastibrand micro PMMA cuvettes were used in the experiment and Zetasizer software (Malvern Instruments) was used to obtain the particle size distributions and derived count rate. Each experiment is the average of three samples, each of one resulting of 14 runs acquired for 10 s each.

*Small angle X-ray scattering:* The aqueous samples were sealed between two Kapton foils. The sample environment was evacuated to reduce background scattering from air. The small-angle X-

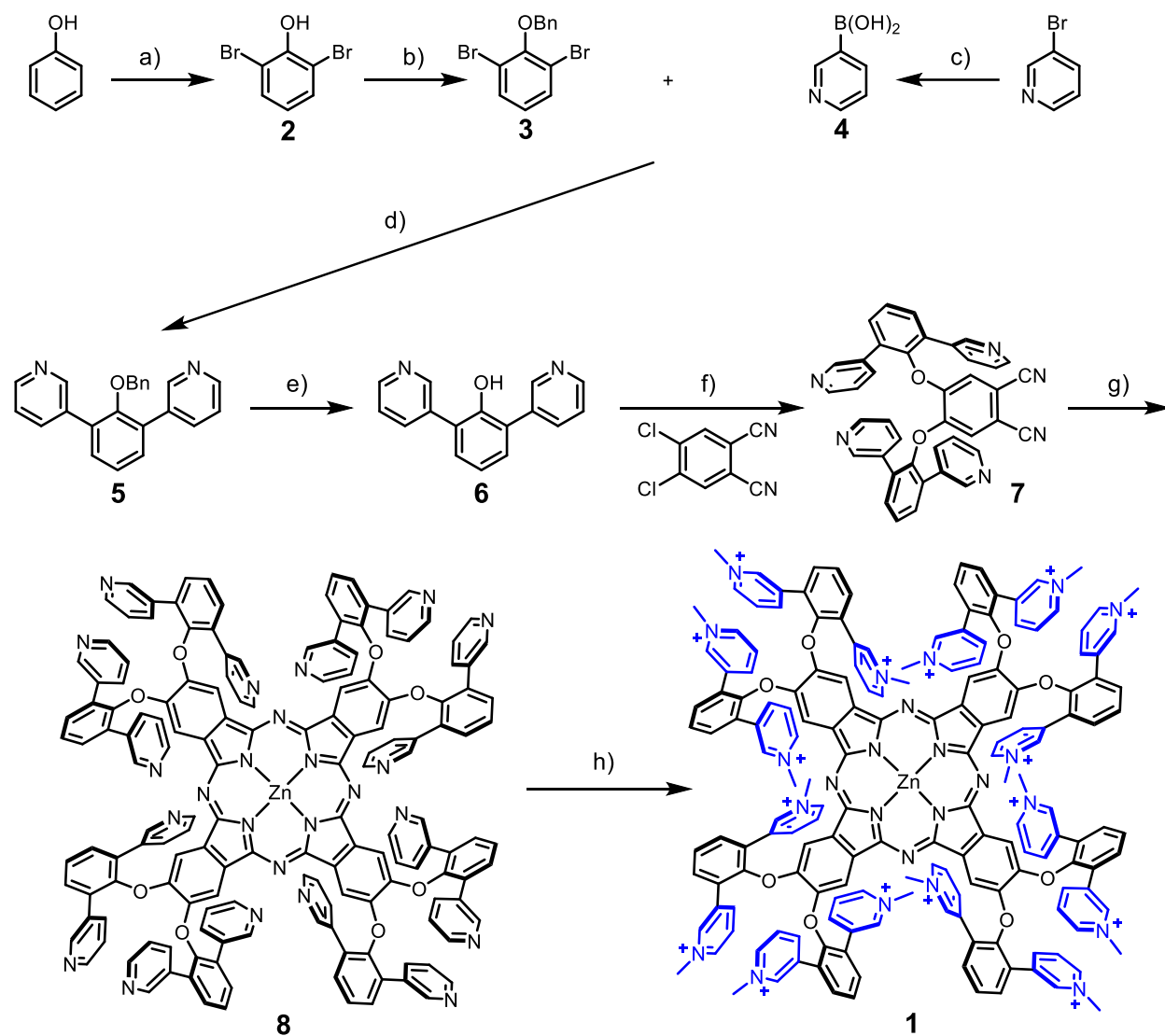
ray scattering (SAXS) was measured using a Bruker Microstar microfocus rotating anode X-ray source (Cu K $\alpha$  radiation,  $\lambda = 1.54 \text{ \AA}$ ). The beam was monochromated and focused by a Montel multilayer focusing monochromator (Incoatec). The X-ray beam was further collimated by four collimation slits (JJ X-ray) resulting in a final spot size of less than 1 mm at the sample position. A Hi-Star 2D area detector (Bruker) was used to collect the scattered intensity. Sample-to-detector distance was 1.59 m, and a silver behenate standard sample was used for the calibration of the length of the scattering vector  $q$ . One-dimensional SAXS data was obtained by azimuthally averaging the 2D scattering data and the magnitude of the scattering vector  $q$  is given by  $q = 4\pi \sin\theta/\lambda$ , where  $2\theta$  is the scattering angle. The measured structure factor  $S(q)$  was obtained by dividing the scattering intensity  $I(q)$  by the  $I(q)$  measured from native TMV at the same concentration.

*Tobacco mosaic virus preparation and characterization:* TMV particles were obtained as described previously.<sup>[5]</sup>

*Synthesis of octacationic ZnPc 9:* this derivative has been prepared according to previously described methods.<sup>[6]</sup>

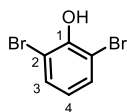
*H<sub>2</sub>DCF pretreatment:* 2',7'-dichlorodihydrofluorescein (H<sub>2</sub>DCF) was obtained by ex-vivo deacetylation of 2',7'-dichlorofluorescein diacetate (H<sub>2</sub>DCFDA) adapting previously reported method.<sup>[7]</sup>

## 2. Synthesis of 1



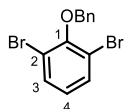
**Scheme S1.** a) NBS,  $(i\text{-Pr})_2\text{NH}$ ;  $\text{CH}_2\text{Cl}_2$ ;  $0^\circ\text{C}$ , 1h; 70%. b) BnCl; 2-Butanone;  $80^\circ\text{C}$ , 2h; 97%. c)  $\text{n-BuLi}$ ,  $(i\text{-Pr})_3\text{B}$ ; Tol/THF (3:1);  $-40^\circ\text{C}$ , 1h; 85%. d)  $\text{Pd(PPh}_3)_4$ ,  $\text{K}_2\text{CO}_3$  (aq., 2 M); DMF;  $120^\circ\text{C}$ , 18 h; 60%. e)  $\text{H}_2$ ,  $\text{Pd(OH)}_2$ ; EtOH; r.t., 6h; 90%. f) 4,5-dichlorophthalonitrile, anh.  $\text{K}_2\text{CO}_3$ ; anh. DMF; microwave reactor,  $125^\circ\text{C}$ , 10 atm., 20 min.; 50%. g)  $\text{Zn(OAc)}_2$ ; DMAE;  $120^\circ\text{C}$ , 18h; 72%. h) Methyl iodide; anh. DMF,  $120^\circ\text{C}$ , 18h, 45%.

## 2,6-dibromophenol (**2**)



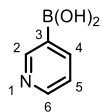
To a solution of 1000 mg of phenol (1 eq, 10.64 mmol) in 50 mL of  $\text{CH}_2\text{Cl}_2$  (4.7 mL  $\text{mmol}^{-1}$ ) was added 0.3 mL of  $(i\text{Pr})_2\text{NH}$  (4.7 mL  $\text{mmol}^{-1}$ ). At 0 °C was added to this solution small portion of NBS (2 eq, 3800 mg, 21.7 mmol). After stirring 1 h at room temperature, aqueous hydrochloric acid (1 M) was added until the solution became acidic. The organic layer was separate and washed with  $\text{H}_2\text{O}$ , dried over  $\text{MgSO}_4$ , filtrated and concentrated *in vacuo*. Compound **2** was purified by chromatography column (eluent heptane/EtOAc 95:5). Compound **2** was obtained with a 70 % yield.  **$^1\text{H-NMR}$**  (300 MHz,  $\text{CDCl}_3$ ):  $\delta$  (ppm) = 7.44 (d, 2H, H-3,  $J$  = 9 Hz); 6.70 (t, 1H, H-4,  $J$  = 9 Hz), 5.88 (s, 1H, -OH).

## 2-(benzyloxy)-1,3-dibromobenzene (**3**)



A solution of 2000 mg of **2** (1 eq, 8 mmol) in 16 mL of 2-butenone (2.6 mL  $\text{mmol}^{-1}$ ) was added 2.0 mL of  $\text{BnCl}$  (2.2 eq, 17.6 mmol) and 2.8 g of anhydrous  $\text{K}_2\text{CO}_3$  (2.5 eq, 20 mmol). The reaction was stirred for 2 hours at reflux. The reaction mixture was cooled to room temperature, filtered, and the solvent was evaporated under reduced pressure. Solid residue was purified by chromatography column (eluent heptane/ $\text{CH}_2\text{Cl}_2$ , 9:1). Compound **3** was obtained with a 97 % yield as a white crystalline solid.  **$^1\text{H-NMR}$**  (300 MHz,  $\text{CDCl}_3$ ):  $\delta$  (ppm) = 7.54 (d, 2H, -Bn,  $J$  = 9 Hz); 7.46 (d, 2H, H-3,  $J$  = 9 Hz); 7.40 (m, 3H, Bn); 6.91 (t, 1H, H-4,  $J$  = 9 Hz); 5.06 (s, 2H, - $\text{CH}_2\text{Ph}$ ).  **$^{13}\text{C-NMR}$**  (74 MHz,  $\text{CDCl}_3$ ):  $\delta$  (ppm) 152.9, 136.3, 132.8, 128.5, 128.4, 126.5, 118.8, 74.64.

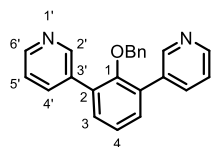
## Pyridine-3-ylboronic acid (**4**)<sup>[8]</sup>



A round-bottomed flask was loaded with 3.5 mL of triisopropyl borate (1.2 eq, 15.20 mmol) and dissolved in previously deoxygenated toluene (16.5 mL, 1.3 mL  $\text{mmol}^{-1}$ ). A second round-bottomed flask was loaded with 2.0 g of 3-bromopyridine (1eq, 12.7 mmol) and previously deoxygenated 5.0 mL of THF (0.4 mL  $\text{mmol}^{-1}$ ). The combination of these two solutions was cooled to -40 °C, followed by dropwise addition of  $n\text{-BuLi}$  (1.6 M, 1.2 eq, 9.5 mL, 15.2 mmol). The reaction mixture was warmed up to -20 °C, followed by addition of 2M  $\text{HCl}$  solution (2 mL). The reaction mixture was allowed to reach room temperature, followed by a pH adjustment to 7 by careful addition of 5M  $\text{NaOH}$  aqueous solution. Resulting mixture was saturated with  $\text{NaCl}$ , and the aqueous phase extracted with THF (3 x 40 mL). The combined organic phases were dried over  $\text{MgSO}_4$ , filtered, and evaporated under reduced pressure. The solid residue was further purified by recrystallization in acetonitrile. Compound **4** was obtained with 85 % yield as a white crystalline solid.  **$^1\text{H-NMR}$**  (300 MHz,  $\text{MeOD-d}_4$ ):  $\delta$  (ppm) = 7.23 (s, 1H, H-2), 7.17 (d, 1H, H-6,  $J$  = 6 Hz), 6.97 (d, 1H, H-4,  $J$  = 6 Hz), 6.26 (bt, 1H, H-5,  $J$  = 6 Hz).

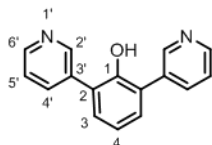


### 1-(benzyloxy)-2,6-(pyridin-3'-yl)benzene (5)



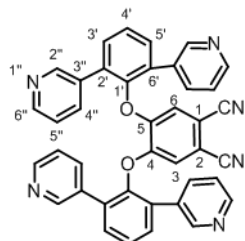
In a round-bottomed flask were added 1000 mg of **3** (1 eq, 2.9 mmol) and 910 mg of **4** (2.5 eq, 7.35 mmol), followed by deoxygenation by several vacuum-argon cycles. Then 15 mL of deaerated DMF (5 mL mmol<sup>-1</sup>) and 9 mL of deaerated K<sub>2</sub>CO<sub>3</sub> (2 M, 3.1 mL mmol<sup>-1</sup>) were added, followed by thorough deoxygenation by argon stream. After 15 min, Pd(PPh<sub>3</sub>)<sub>4</sub> was added, and the mixture was heated to 120 °C during 18 hours. The reaction mixture was left to cool down to room temperature, followed by solvent removal under reduced pressure. The solid residue was dissolved in a mixture of CHCl<sub>3</sub> and water. The aqueous phase was washed further with CHCl<sub>3</sub> (3x10 mL). The combined organic layers were dried over MgSO<sub>4</sub>, filtered, and evaporated under reduced pressure. The solid residue was purified by chromatography column (eluent CH<sub>2</sub>Cl<sub>2</sub>/EtOAc, 1:1). Compound **5** was obtained with a 60 % yield as a white crystalline solid. **<sup>1</sup>H-NMR** (300 MHz, CDCl<sub>3</sub>): δ (ppm) = 8.70 (dd; 2H; H-2'; *J*<sub>1</sub> = 3 Hz, *J*<sub>2</sub> = 1 Hz), 8.48 (dd; 2H; H-6'; *J*<sub>1</sub> = 3 Hz, *J*<sub>2</sub> = 1 Hz), 7.81 (dt; 2H; H-5'; *J*<sub>1</sub> = 6 Hz, *J*<sub>2</sub> = 3 Hz), 7.24 (m; 4H), 6.98 (m, 3H), 6.50 (dd; 2H; H-Bz; *J*<sub>1</sub> = 6 Hz, *J*<sub>2</sub> = 3 Hz), 4.03 (s, 2H, -CH<sub>2</sub>Bz). **<sup>13</sup>C-NMR** (74 MHz, CDCl<sub>3</sub>): δ (ppm) = 150.1, 148.6, 137.0, 135.6, 134.0, 133.2, 132.2, 132.0, 131.9, 131.9, 130.8, 129.5, 128.9, 128.5, 128.4, 128.1, 128.1, 125.2, 123.3, 123.0, 122.6, 75.4. **HRMS (ESI)** *m/z*: [M]<sup>+</sup> calcd for C<sub>23</sub>H<sub>18</sub>N<sub>2</sub>O, 338.1419; found, 338.1406.

### 2,6'-(bis(pyridin-3-yl))phenol (6)



To a solution of 75 mg of **5** (1 eq, 0.3 mmol) in 3.5 mL of EtOH (12 mL mmol<sup>-1</sup>) were added 18 mg of Pd(OH)<sub>2</sub> (61 mg of Pd(OH)<sub>2</sub> mmol<sup>-1</sup> of **5**). The mixture was stirred overnight under H<sub>2</sub> atmosphere (1 atm, balloon) at room temperature. The reaction mixture was filtered through Celite, using MeOH as solvent, and evaporated under reduced pressure. Reaction crude was purified by chromatography column (eluent CH<sub>2</sub>Cl<sub>2</sub>: MeOH, 95:5). Compound **6** was obtained with a 90 % yield as a white crystalline solid. **<sup>1</sup>H-NMR** (300 MHz, CDCl<sub>3</sub>): δ (ppm) = 8.77 (bs; 2H; H-2'), 8.52 (d; 2H; H-6'; *J* = 6 Hz), 7.92 (bd; 2H; H-4'; *J* = 6 Hz), 7.38 (dd; 2H; H-5'; 2H; *J*<sub>1</sub> = 6 Hz, *J*<sub>2</sub> = 6 Hz), 7.29 (m; 4H; H-3 and H-5'), 7.13 (t; 1H; H-4; *J*<sub>1</sub> = 6 Hz), 5.31 (s, 1H, -OH). **<sup>13</sup>C-NMR** (74 MHz, CDCl<sub>3</sub>): δ (ppm) = 150.6, 150.3, 148.7, 137.1, 133.8, 131.0, 126.4, 123.6, 121.4. **HRMS (ESI)** *m/z*: [M]<sup>+</sup> calcd for C<sub>16</sub>H<sub>12</sub>N<sub>2</sub>O, 248.0950; found, 248.0954.

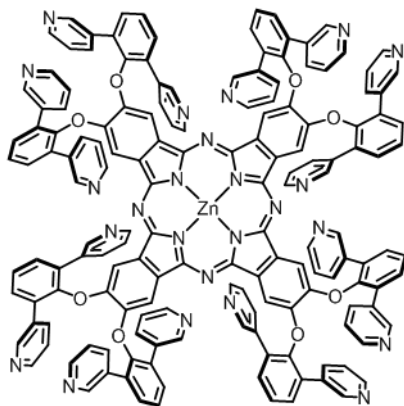
### 4,5-bis(-2,6-di(pyridin-3-yl)phenyl)phthalonitrile (7)



To a 5 mL microwave vial were added 200 mg of **6** (2.5 eq, 0.8 mmol), 63 mg of 4,5-dichlorophthalonitrile in 1.3 mL of dry DMF (4 mL mmol<sup>-1</sup>). When this solution was homogenized 222 mg of dry potassium carbonate (5 eq, 1.61 mmol) were added. The reaction tube was sealed and heated to 125 °C under microwave irradiation (100% of power and 10 atm of pressure). The reaction crude was poured over water and the solid was filtered under vacuum. Compound **7** was purified by flash column chromatography (eluent CH<sub>2</sub>Cl<sub>2</sub>: MeOH, 97.5:2.5). Compound **7** was obtained with a 50 % yield as a white crystalline solid. **<sup>1</sup>H-NMR** (300 MHz, CDCl<sub>3</sub>): δ (ppm) = 8.65 (bs; 4H; H-2''), 8.48 (d; 4H; H-6''; *J* = 6 Hz), 7.63 (bd; 4H; H-4''; *J* = 6 Hz), 7.50 (m; 6H; H-3' and H-4'), 7.00 (dd; 2H; H-5''; 4H; *J*<sub>1</sub> = 3 Hz, *J*<sub>2</sub> = 1 Hz), 6.36 (s, 2H, H-3). **<sup>13</sup>C-NMR** (74 MHz, CDCl<sub>3</sub>): δ (ppm) = 149.6, 149.4, 148.22, 147.0, 136.0,

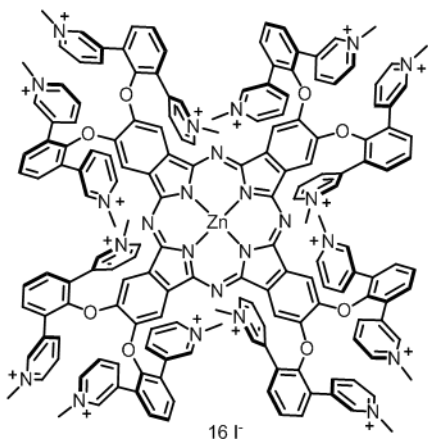
132.5, 132.2, 131.8, 127.6, 123.1, 119.5, 114.2, 108.8. **HRMS (ESI)**  $m/z$ :  $[M]^+$  calcd for  $C_{40}H_{24}N_6O_2$ , 621.2033; found, 621.2038.

### Zinc(II)phthalocyanine (**8**)\*



To a solution of 120 mg of **7** (4 eq, 0.18 mmol) in 0.53 mL of DMAE (3 mL mmol<sup>-1</sup>) under argon in a small sealed tube were added 17 mg of Zn(OAc)<sub>2</sub> (2 eq, 0.09 mmol). The mixture was stirred overnight at 120 °C. The reaction mixture was cooled at room temperature and poured in water (20 mL). The green precipitate was collected by filtration and washed with H<sub>2</sub>O and a mixture of water/MeOH (1:1). Compound **8** was purified by biod bead chromatography using CHCl<sub>3</sub> as eluent. Compound **8** was obtained with a 72 % yield as a green solid. **<sup>1</sup>H-NMR** (300 MHz, CDCl<sub>3</sub>+1% pyridine):  $\delta$  (ppm) = 8.92 (bs; 16H; H-2''), 8.17 (d; 16H; H-6'');  $J$  = 8 Hz), 7.91 (bd; 16H; H-5'');  $J$  = 6 Hz), 7.83 (s; 8H; H-Pc), 7.72 (bs; 24H; H-3' and H-4'), 6.84 (dd; 16H; H-4'');  $J_1$  = 6 Hz,  $J_2$  = 3 Hz). **ESIMS**  $m/z$  (%): 2546.7 (100)  $[M]^+$ .

### Hexadecacationic Zn(II)phthalocyanine (**1**)\*



To a solution of 62 mg of **8** (1 eq, 0.024 mmol) in 7.3 mL of dry DMF (300 mL mmol<sup>-1</sup>) under argon in a small sealed tube were added 0.16 mL of methyl iodide (70 eq, 1.7 mmol). The mixture was stirred overnight at 120 °C. The reaction mixture was cooled at room temperature and poured in MeOH (20 mL). The green precipitate was collected by filtration and washed with MeOH. Compound **ZnPc(16+)** was obtained with a 45 % yield as a green solid. **<sup>1</sup>H-NMR** (300 MHz, DMSO-*d*<sub>6</sub>):  $\delta$  (ppm) = 9.59 (bs; 16H; H-2''), 8.60 (d; 16H; H-6'');  $J$  = 8 Hz), 8.41 (m; 24H; H-4'' and H-Pc), 8.01 (d; 16H; H-3',  $J$  = 9 Hz), 7.87 (t; 8H; H-4',  $J$  = 9 Hz), 7.79 (t; 16H; H-5'');  $J$  = 8 Hz). **ESIMS**  $m/z$  (%): 543.57 (100)  $[M^{16+} - 16I^- + 9TFA^-]^{7+}$ , 652.99 (85)  $[M^{16+} - 16I^- + 10TFA^-]^{6+}$ , 806.19 (45)  $[M^{16+} - 16I^- + 11TFA^-]^{5+}$ , 1035.98 (21)  $[M^{16+} - 16I^- + 12TFA^-]^{4+}$ , 1418.97 (16)  $[M^{16+} - 16I^- + 13TFA^-]^{3+}$ , 1507.61 (9)  $[M^{16+} - 16I^- + 15TFA^- + Ca^{2+}]^{3+}$ . **HRMS (ESI)**  $m/z$ :  $[M^{16+} - 16I^- + 9TFA^-]^{7+}$  calcd for  $(C_{176}H_{144}N_{24}O_8)(C_2O_2F_3)_9$ , 543.5651; found, 543.5652.

\* <sup>1</sup>H-NMR numeration has not been included for clarity purposes, being the same as compound **6**.

### 3. Aggregation in NaCl concentrations

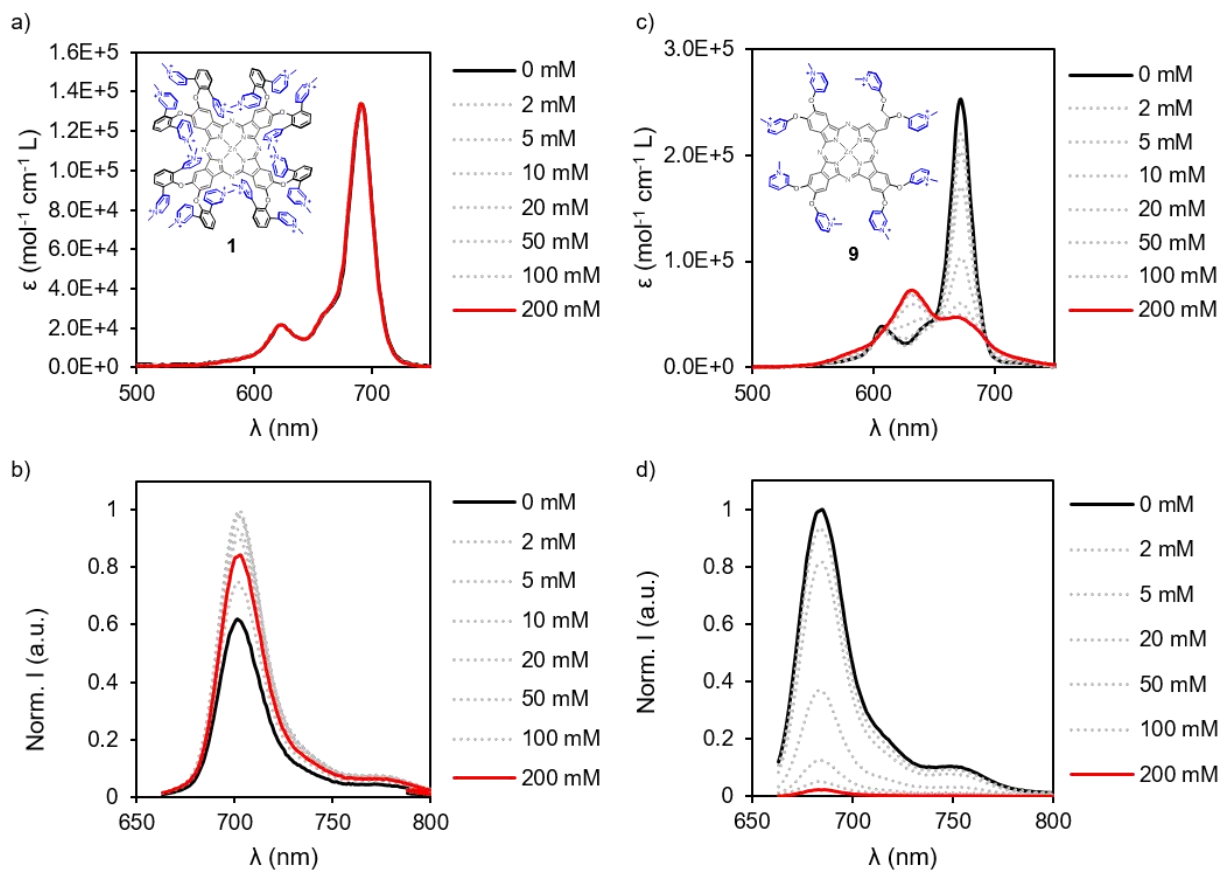


**Figure S1.** Absorbance (a) and normalized emission (b) of **1** and reference **9** (c and d, respectively) in increasing NaCl concentration at  $2 \times 10^{-6}$  M. Emission recorded with  $\lambda_{\text{exc}} = 615$  nm.

#### 4. Fibers dissociation

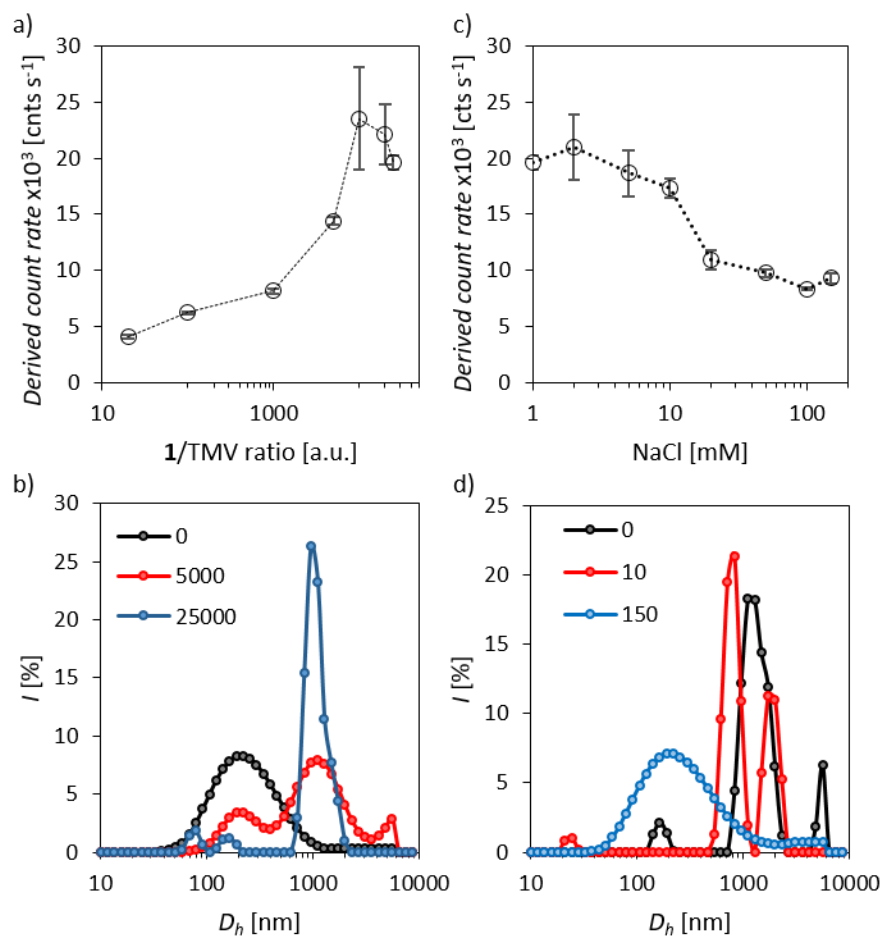


**Figure S2.** Derived count rate (a) and DLS intensity profiles of TMV at 0.1 mg mL<sup>-1</sup> (b) upon addition of increasing equivalents of **1**, followed by immediate dissociation at increasing amount of NaCl (c and d) in mM.

## 5. 1-TMV conjugates

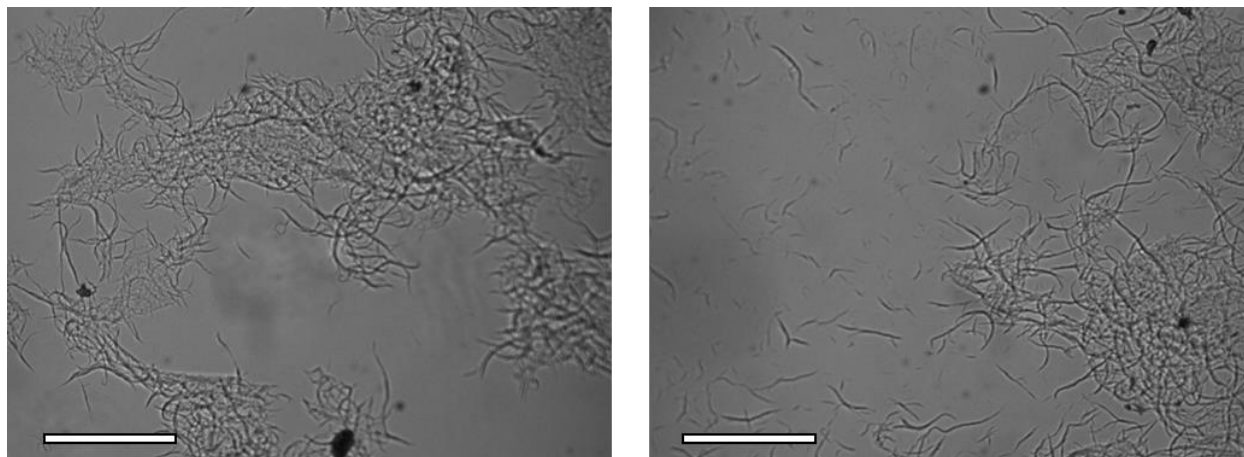


**Figure S3.** Optical images of 1-TMV fibers obtained by mixing both components in acetate buffer 10 mM pH 5.5, in absence of NaCl. *Scale bar:* 100  $\mu\text{m}$ .

## 6. Angle variation under cross polarizers

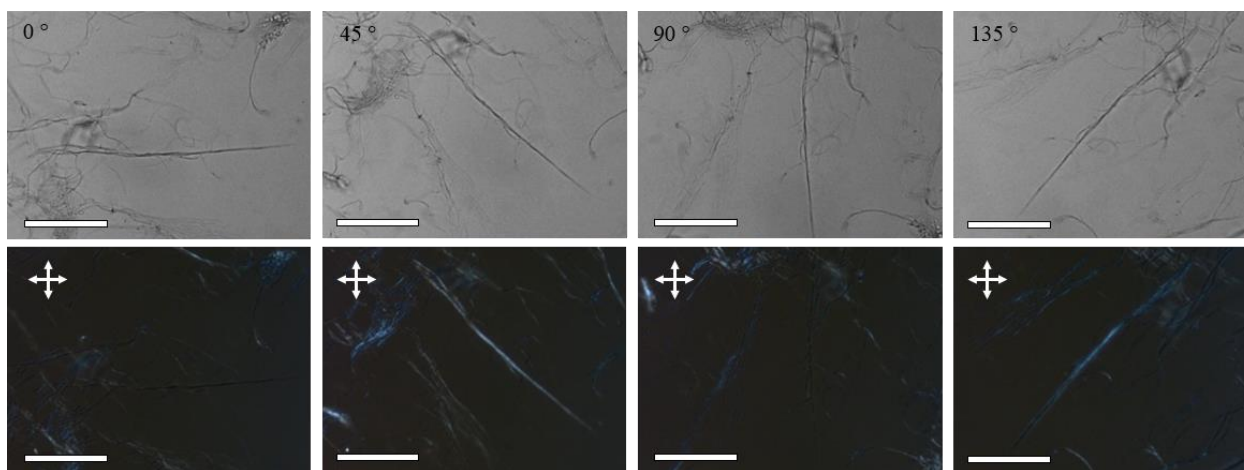


**Figure S4.** Optical (top) and polarized light (bottom) microscopy images. The fiber is aligned at the angle showed in the top-left corner of the optical image. The latter was taken between cross-polarizers, align as shown in top-left corner vectors in each image. *Scale bar:* 100  $\mu\text{m}$ .

## 7. ROS controls

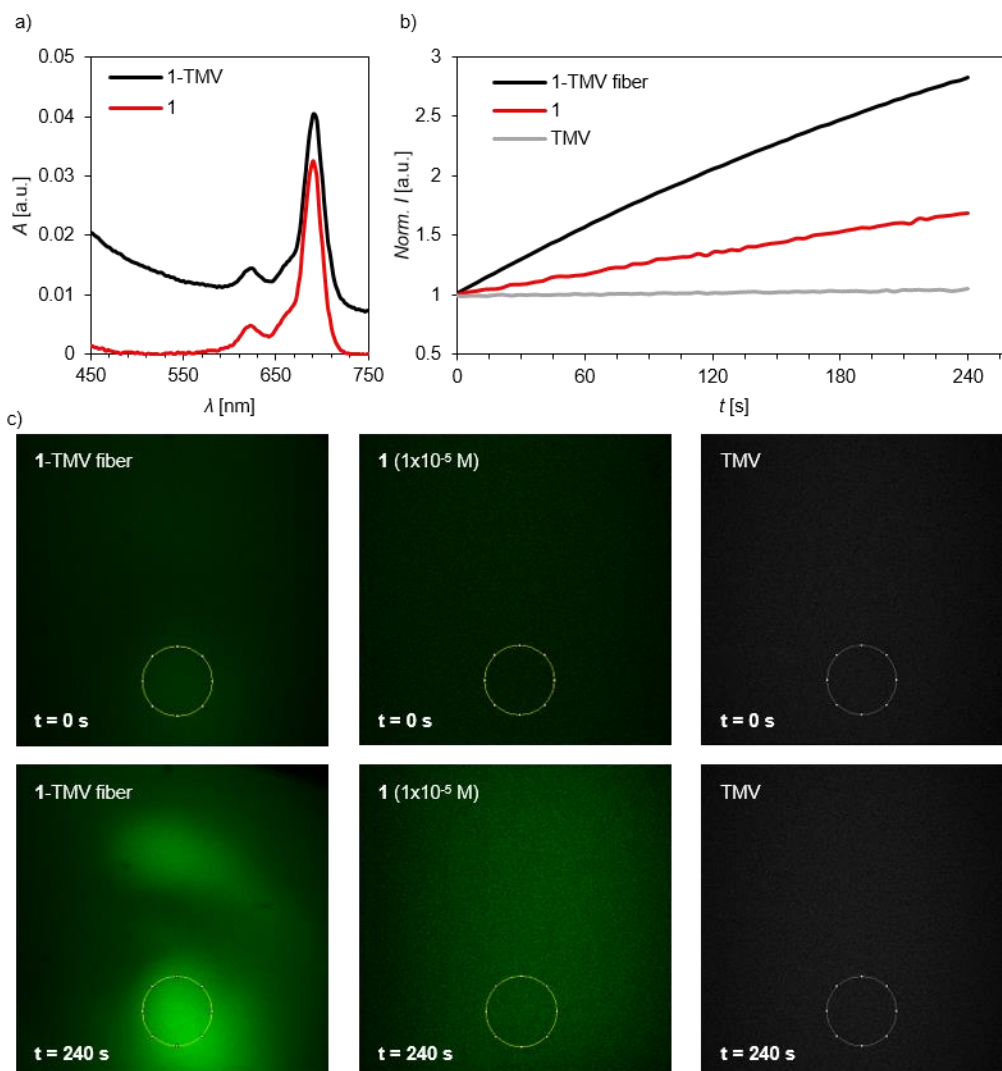


**Figure S5.** (a) Absorption of **1**-TMV fibers (black) and **1** at  $1 \times 10^{-5}$  M (red). (b) Normalized increase of DCF emission (750  $\mu$ m) in presence of the biohybrids (black), **1** at  $1 \times 10^{-5}$  M (red) and TMV (grey). (c) Micrographs of the aforementioned samples displaying the selected ROI for intensity integration at time 0 (top) and 240 s (bottom). All samples were carried out in acetate buffer (10 mM pH = 5.5)

## 8. Oxygen dependence

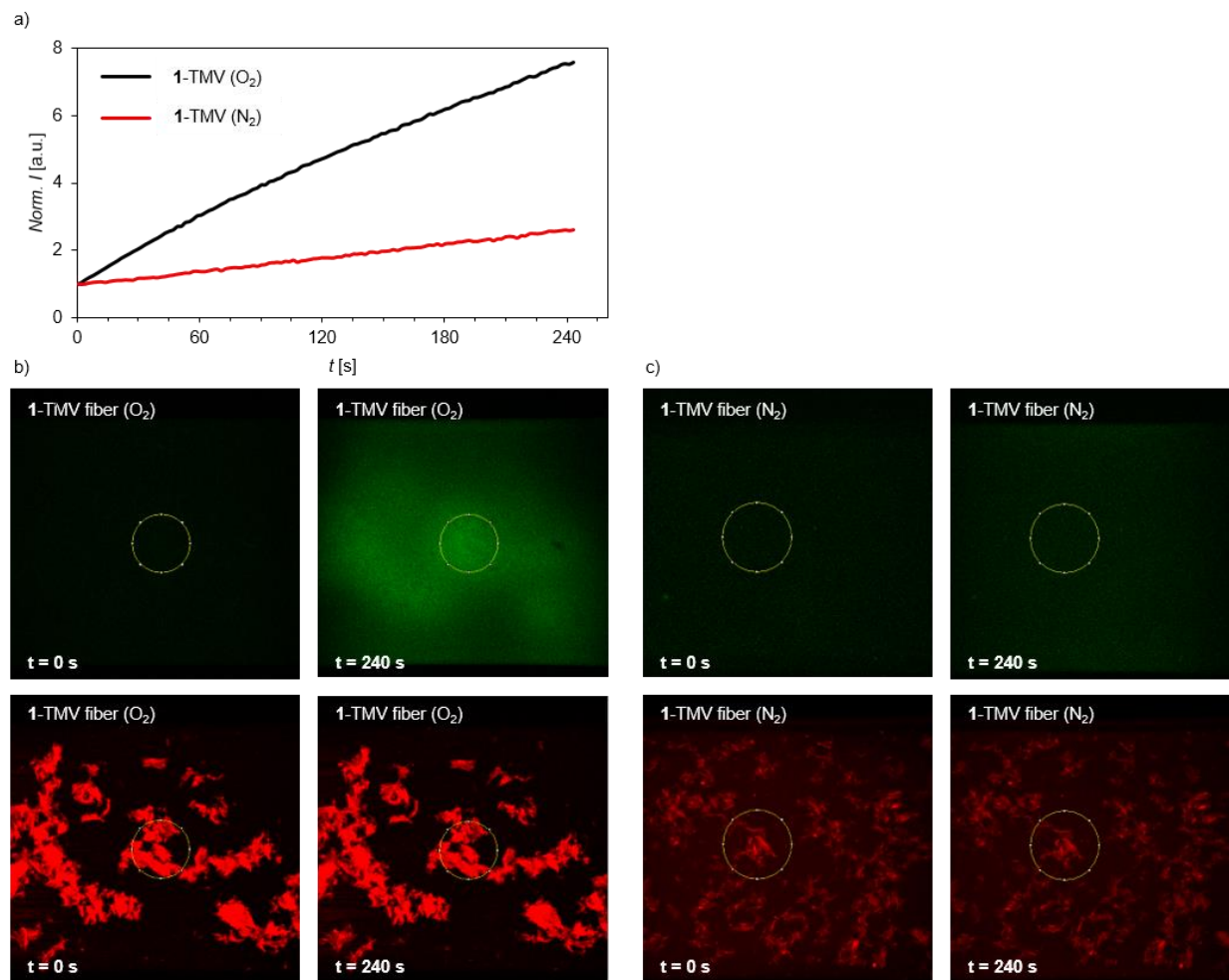


**Figure S6.** (a) Normalized increase of DCF emission (750  $\mu\text{M}$ ) in presence of the biohybrids and oxygen (black) and nitrogen (red). Micrographs of the biohybrid samples (bottom) and DFC (top) in presence of  $\text{O}_2$  (b) and  $\text{N}_2$  (c). All samples were carried out in acetate buffer (10 mM pH = 5.5) and display the selected ROI for intensity integration.

## 9. Proof-of-concept device

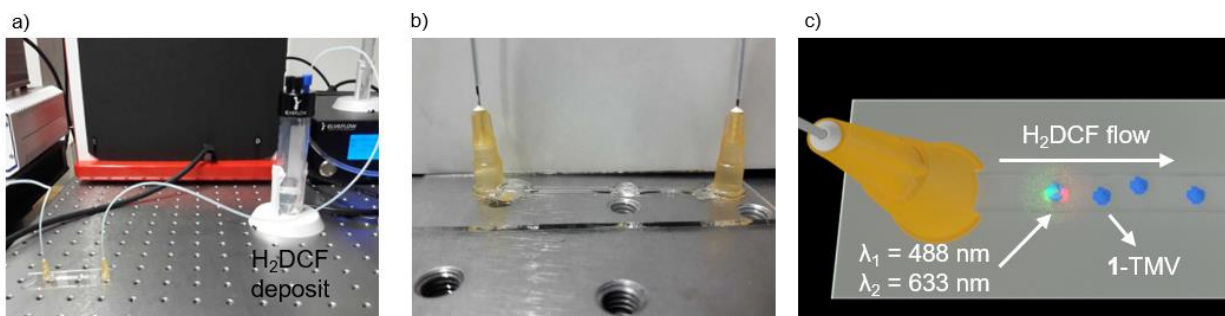


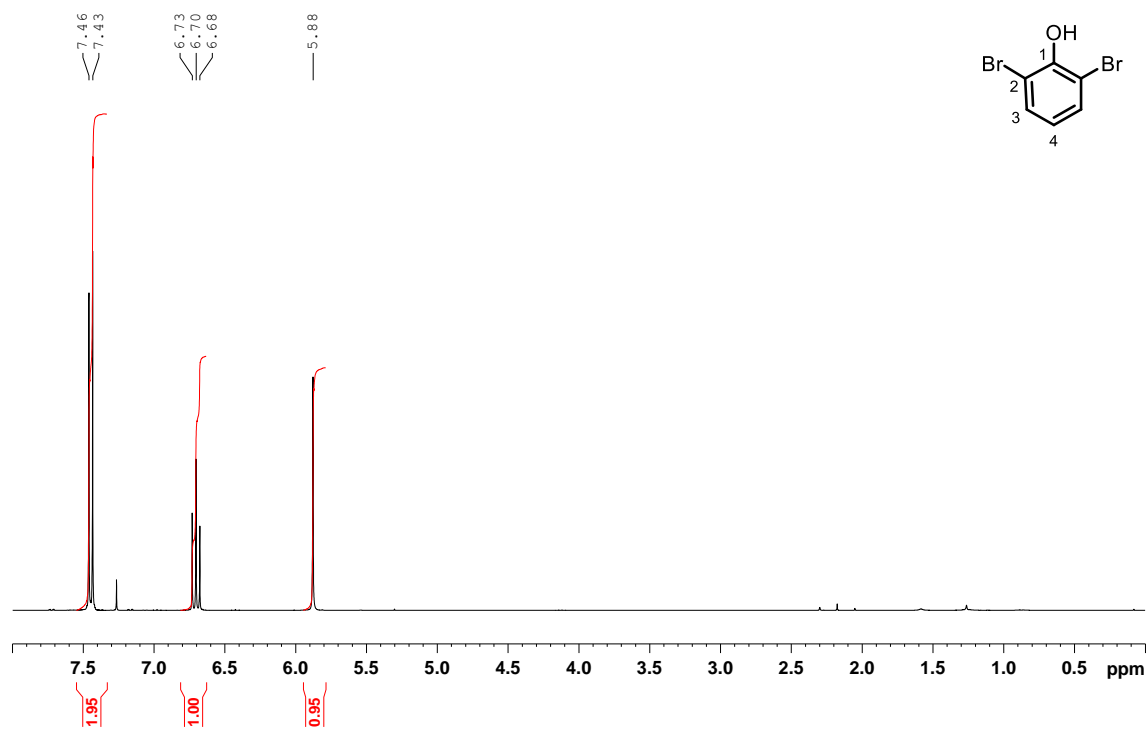
**Figure S7.** (a) Continuous flow device showing the H<sub>2</sub>DCF deposit used to feed the capillary. (b) Detailed image of the square cross-section capillary immobilized on top of a glass slide. (c) Schematic representation of the immobilized 1-TMV bundles and the laser irradiation achieved by the confocal microscope.



## 10. Characterization spectra

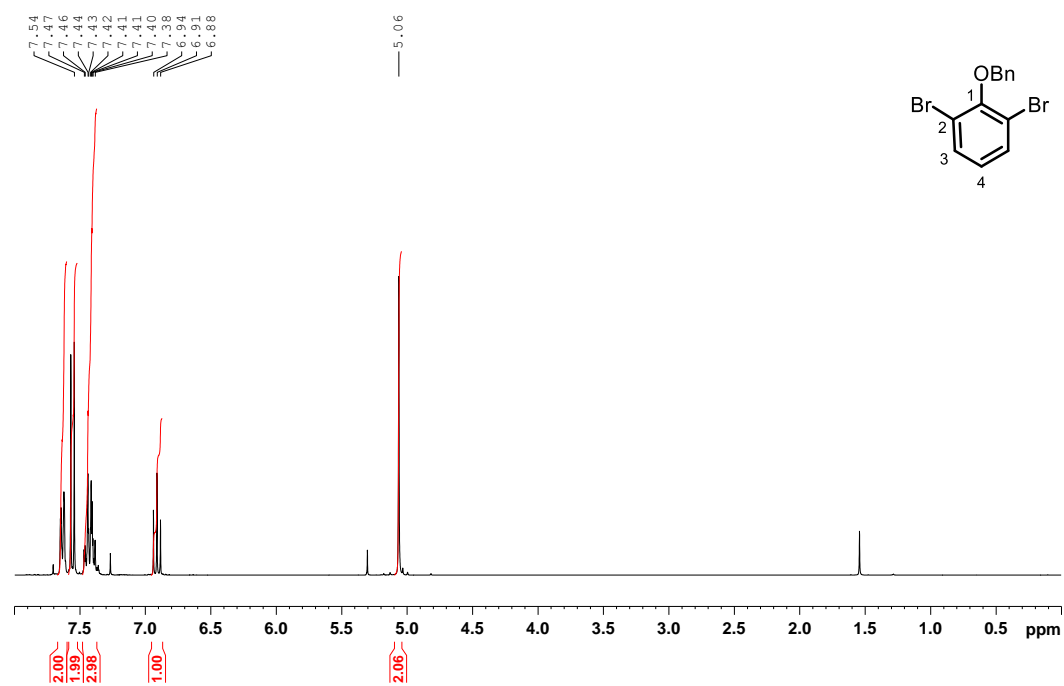
### 2,6-dibromophenol (2)

$^1\text{H-NMR}$ ,  $\text{CDCl}_3$ , 300 MHz.

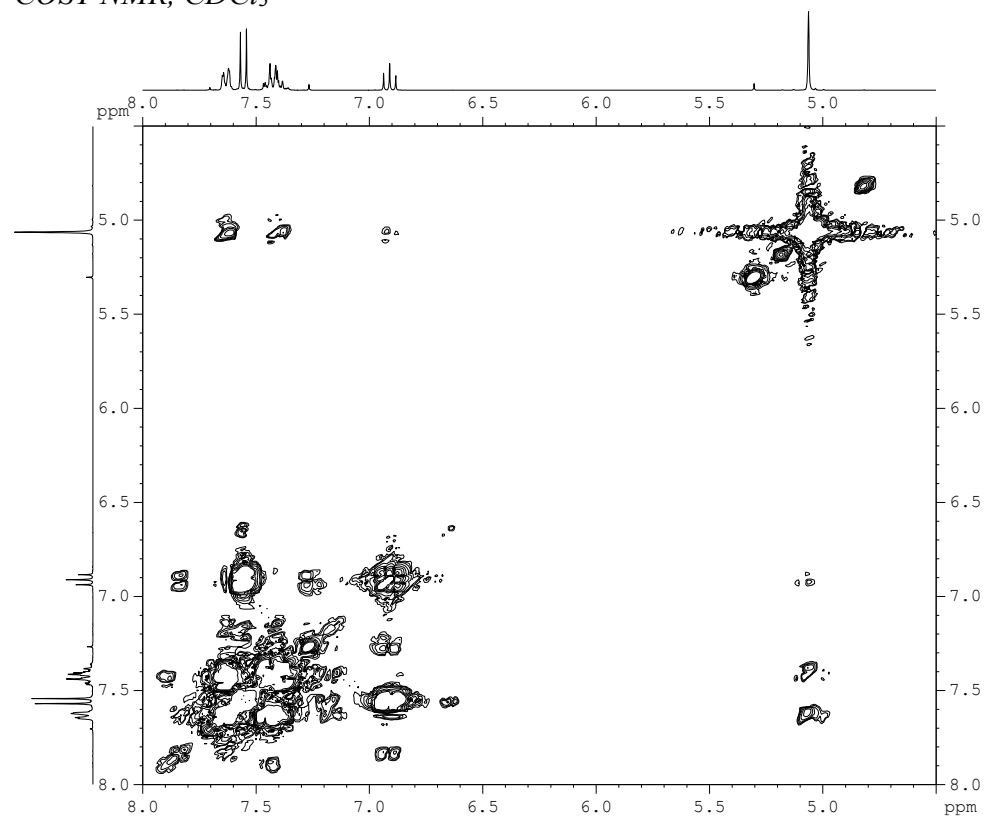


2-(benzyloxy)-1,3-dibromobenzene (3)

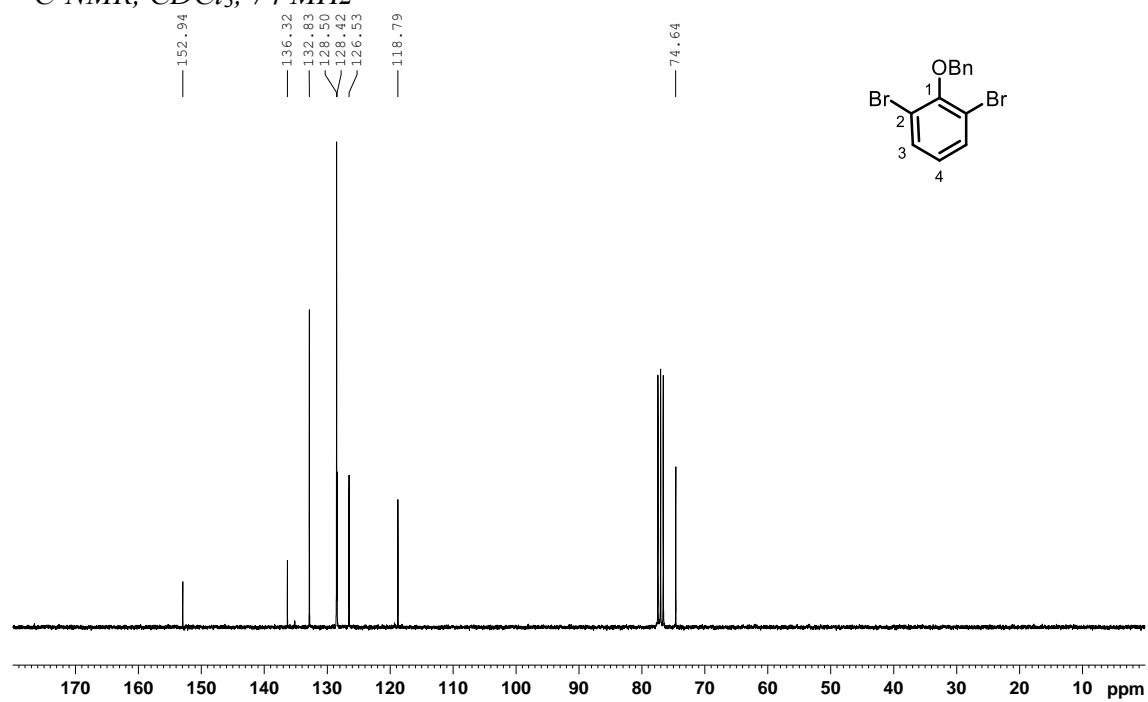
$^1\text{H-NMR}$ ,  $\text{CDCl}_3$ , 300 MHz



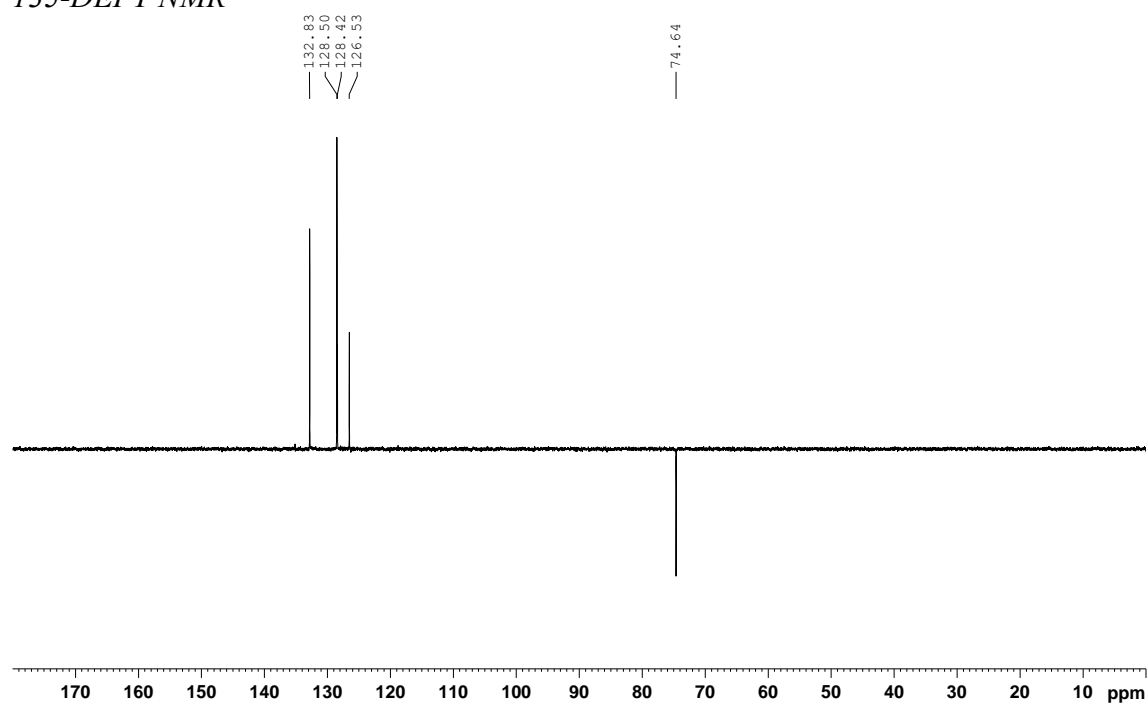
$\text{COSY NMR}$ ,  $\text{CDCl}_3$



$^{13}\text{C}$ -NMR,  $\text{CDCl}_3$ , 74 MHz

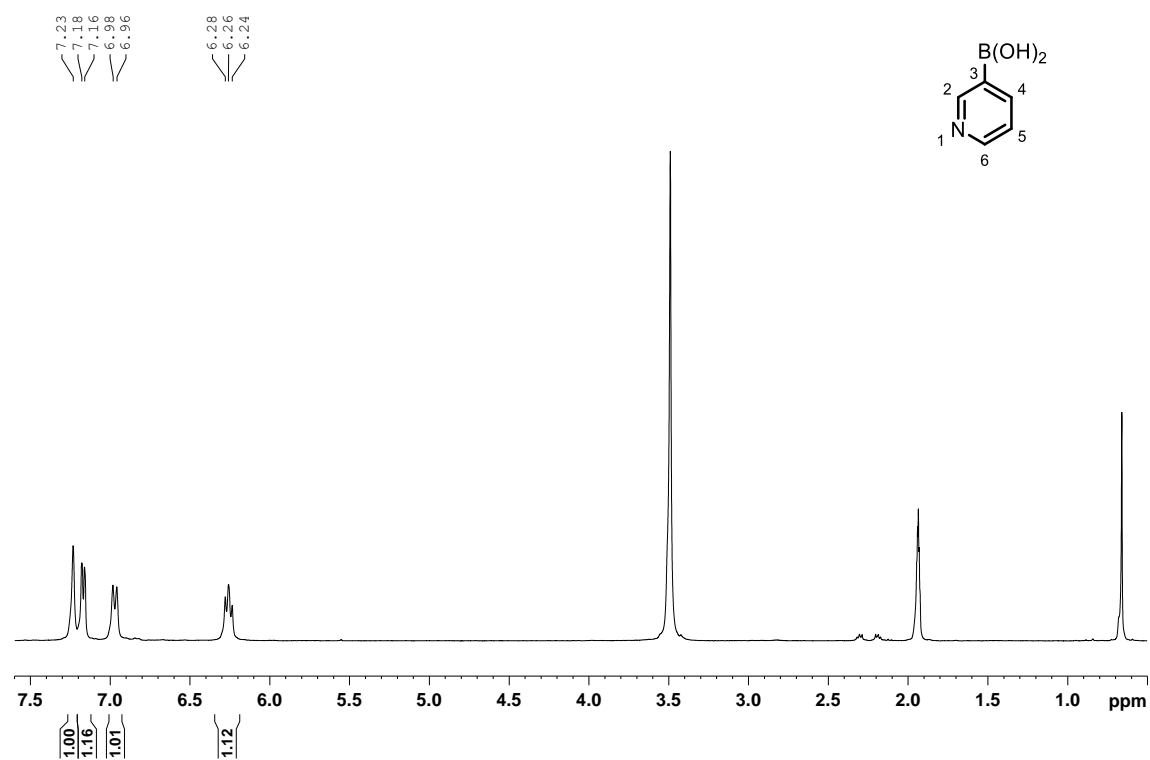


$^{135}\text{-DEPT}$  NMR



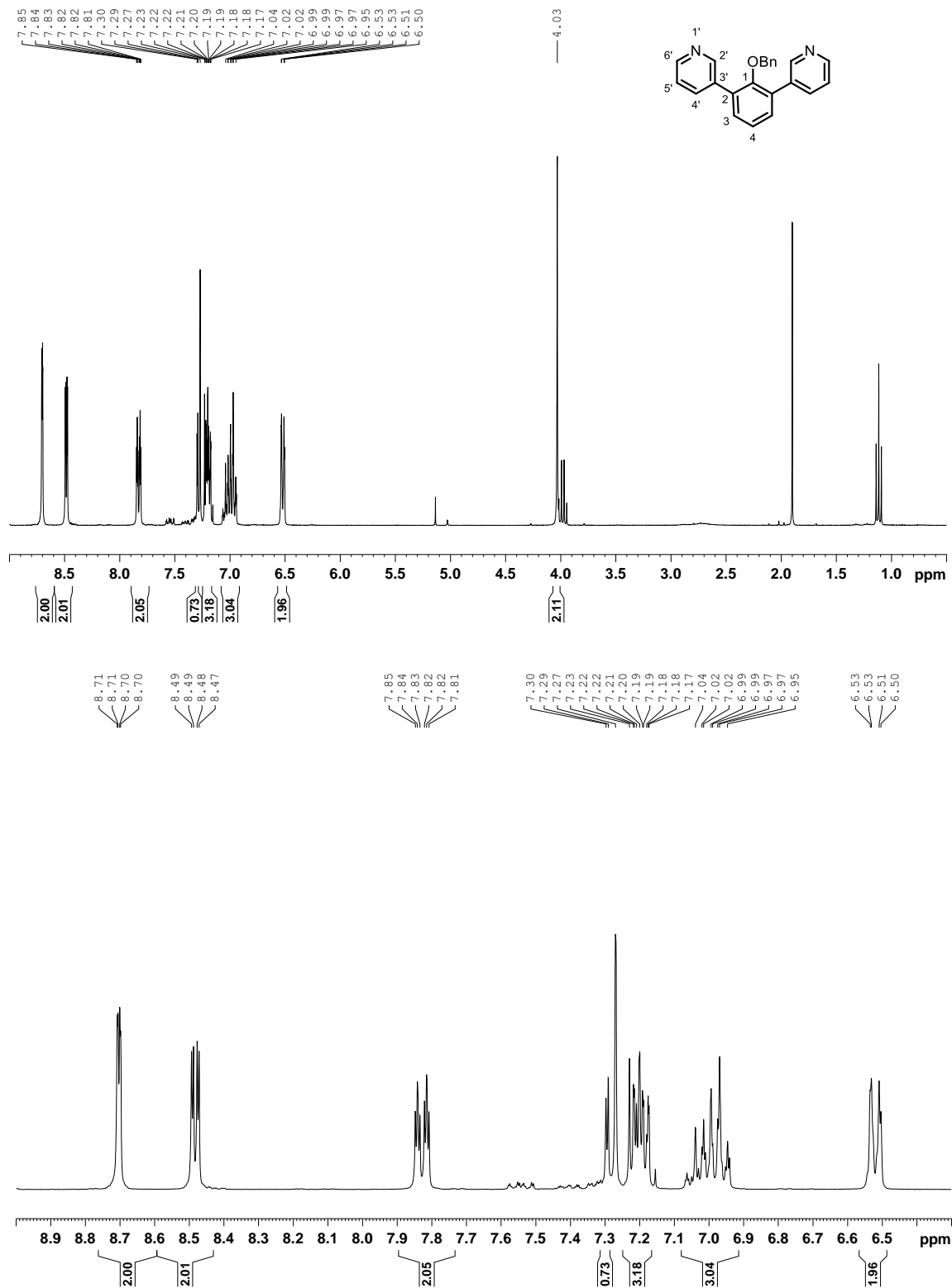
Pyridine-3-ylboronic acid (4)

$^1\text{H-NMR}$ ,  $\text{DMSO-}d_6$ , 300 MHz

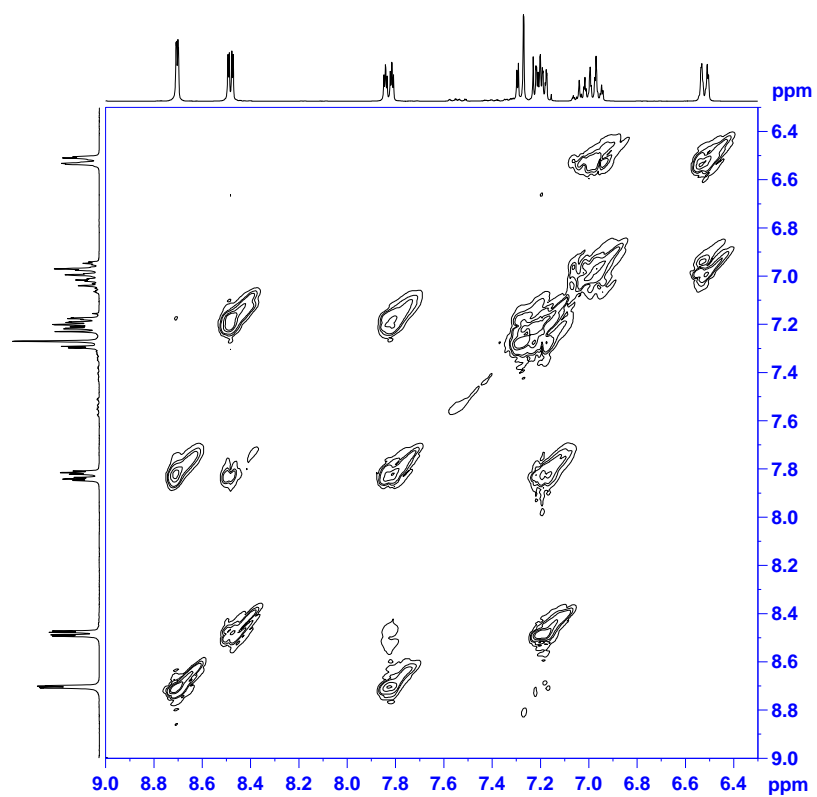
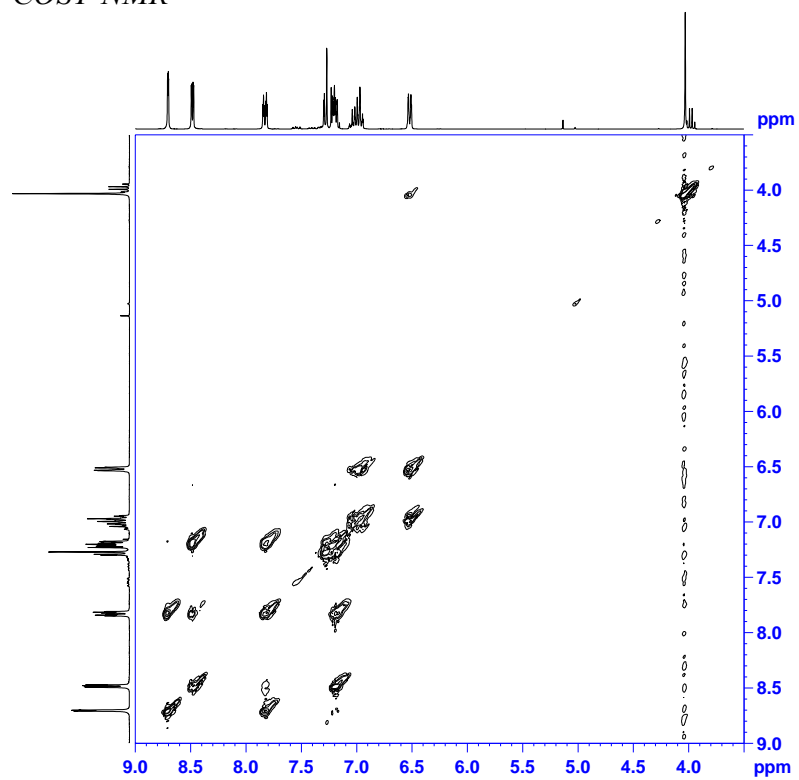


Benzyloxy-2,6-(pyridyn-3'-yl)benzene (5)

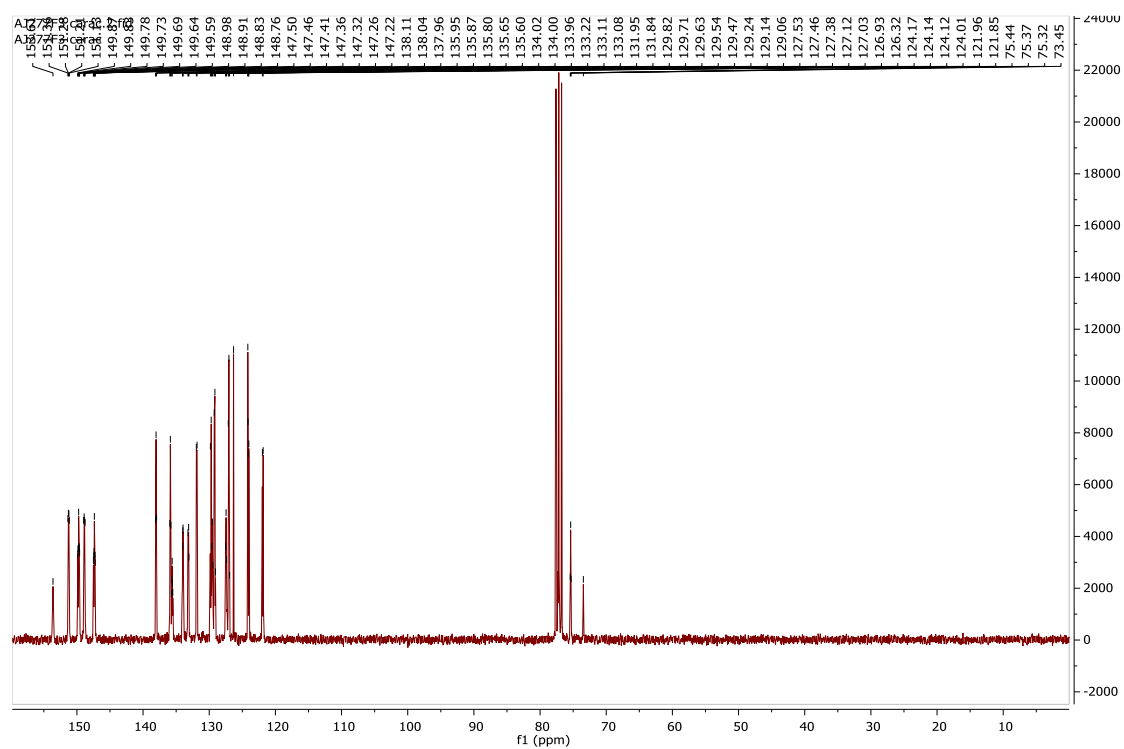
$^1\text{H-NMR}$ ,  $\text{CDCl}_3$ , 300 MHz



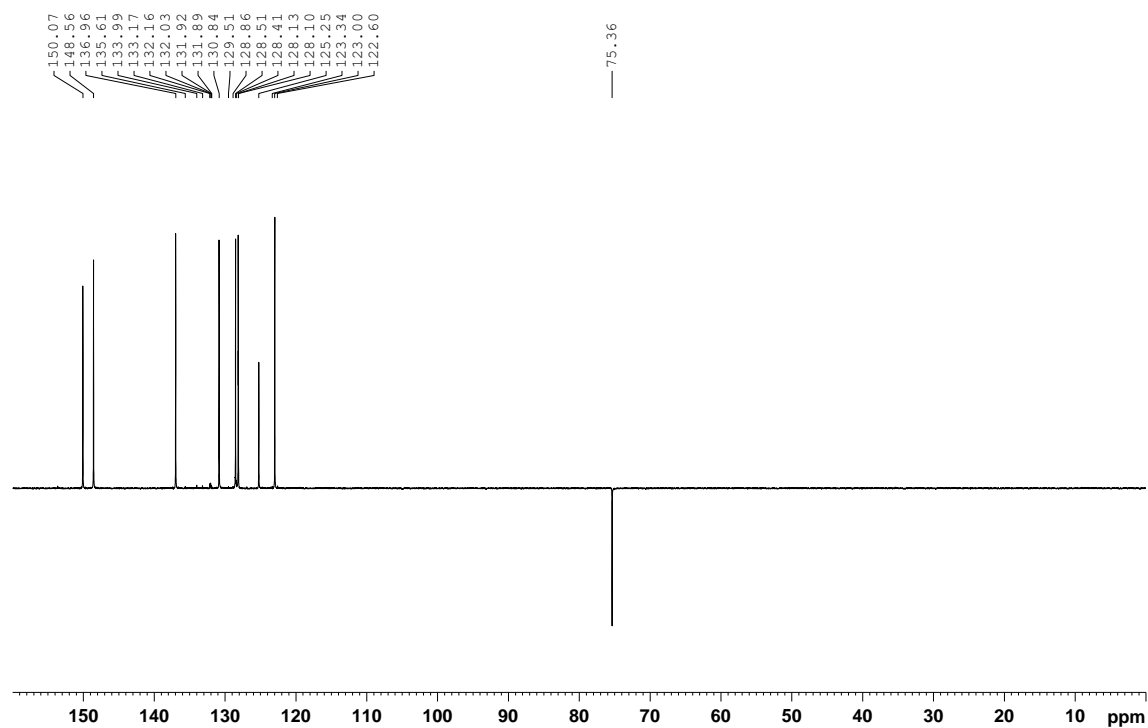
*COSY-NMR*



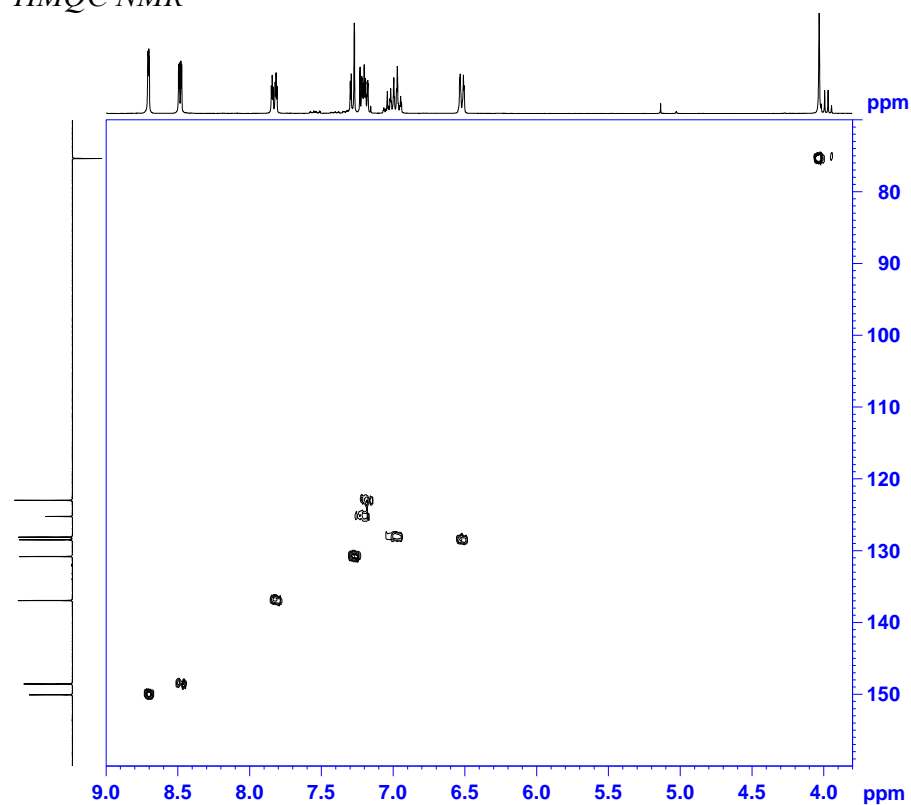
$^{13}\text{C-NMR}$ ,  $\text{CDCl}_3$ , 74 MHz



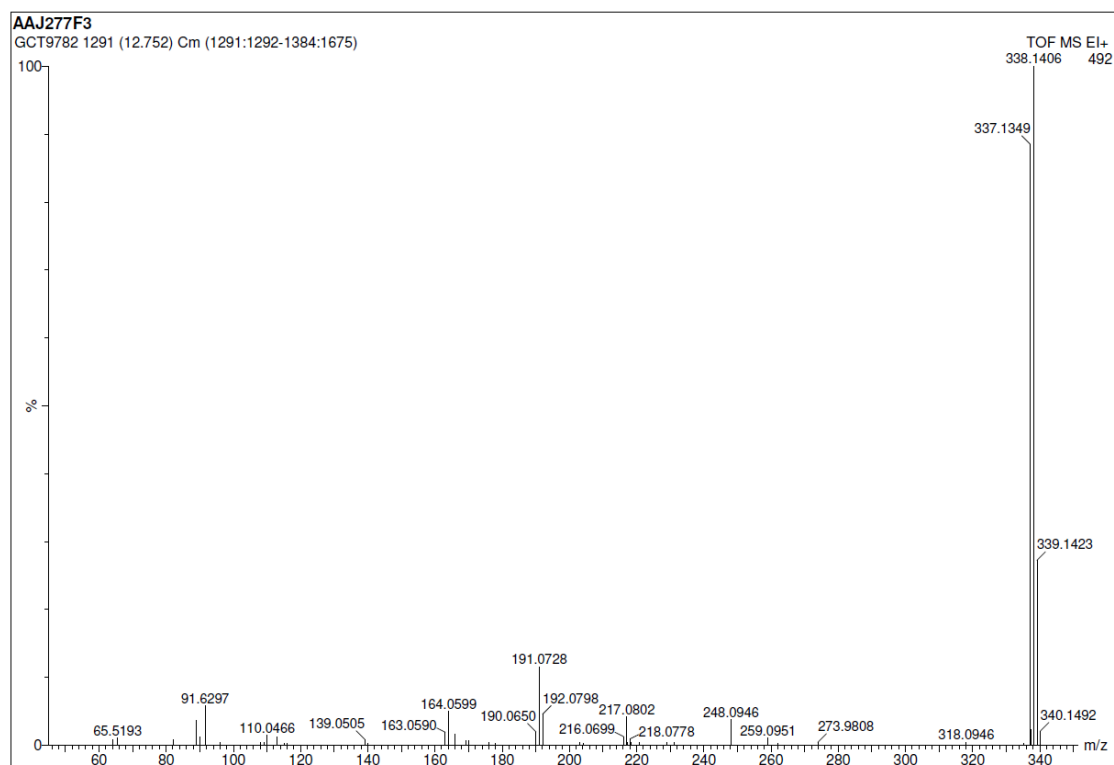
$^{135}\text{-DEPT NMR}$



# *HMQC NMR*



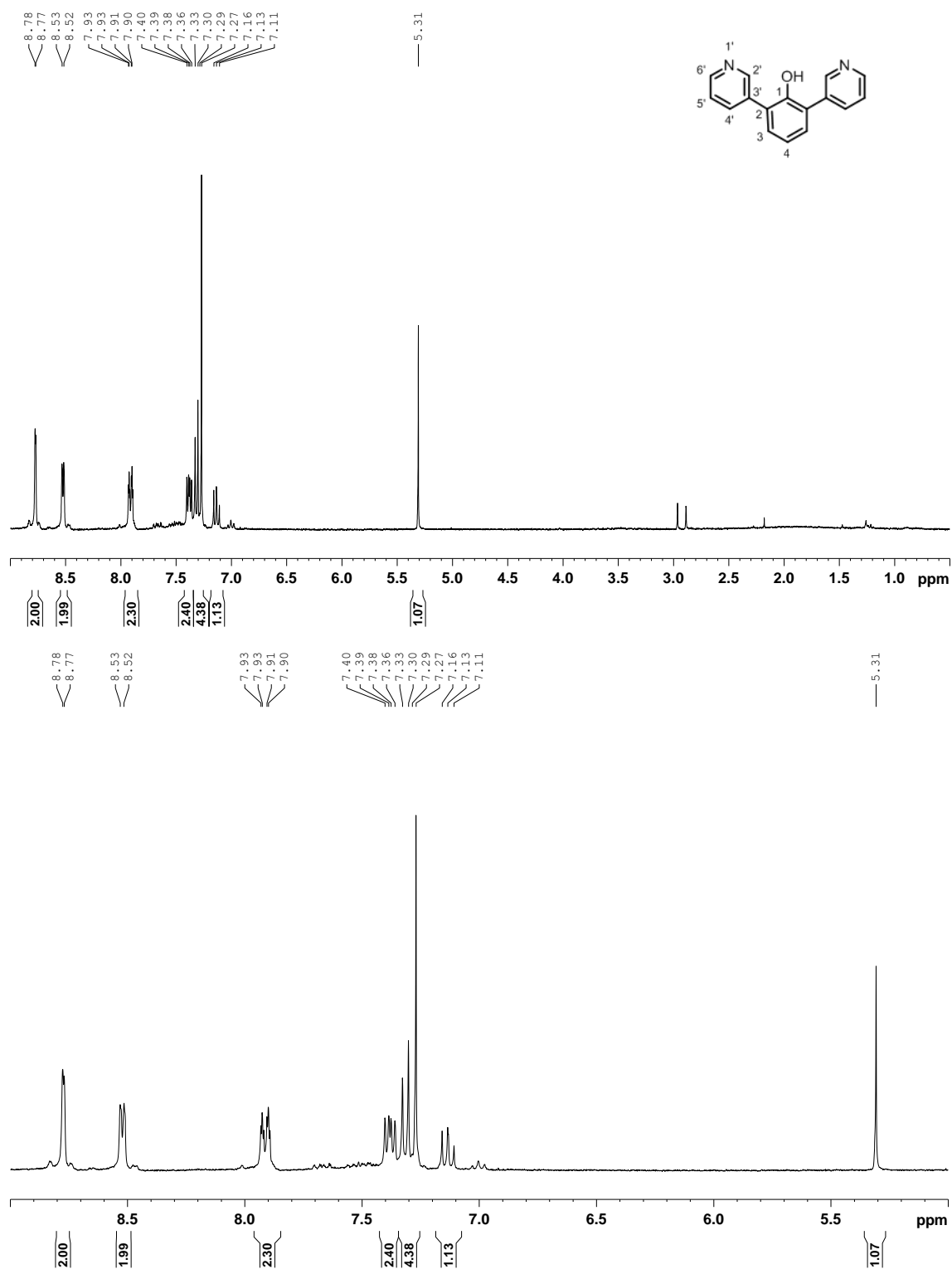
# *ESI mass spectrum*



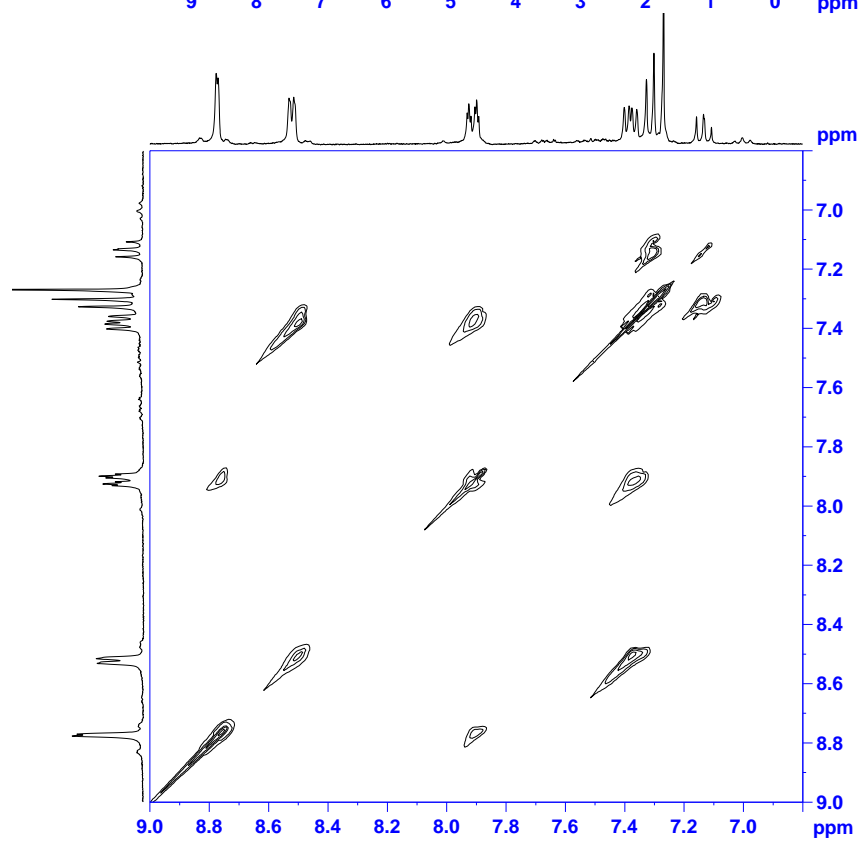
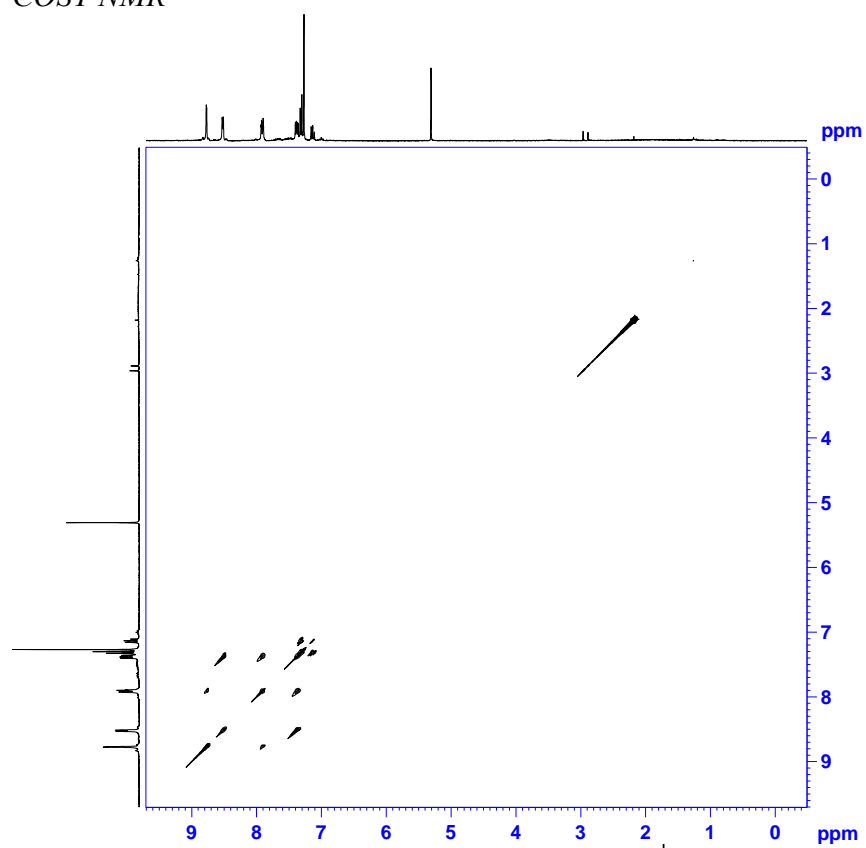


2,6'-(bis(pyridin-3-yl))phenol (6)

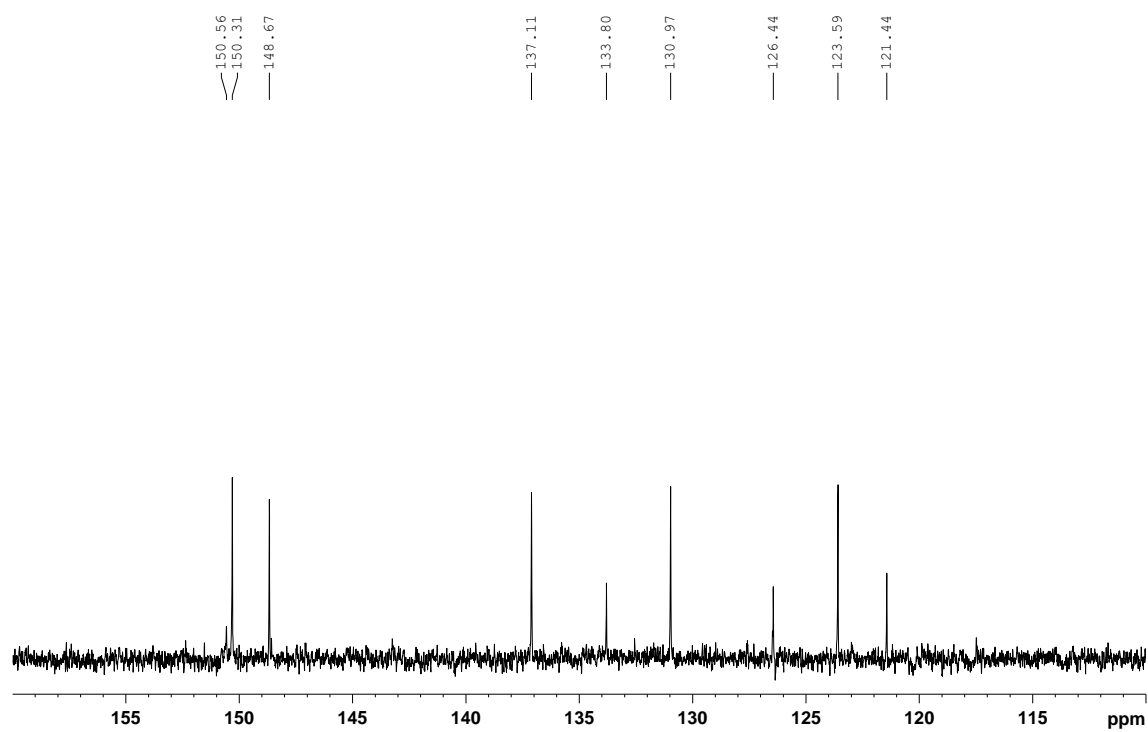
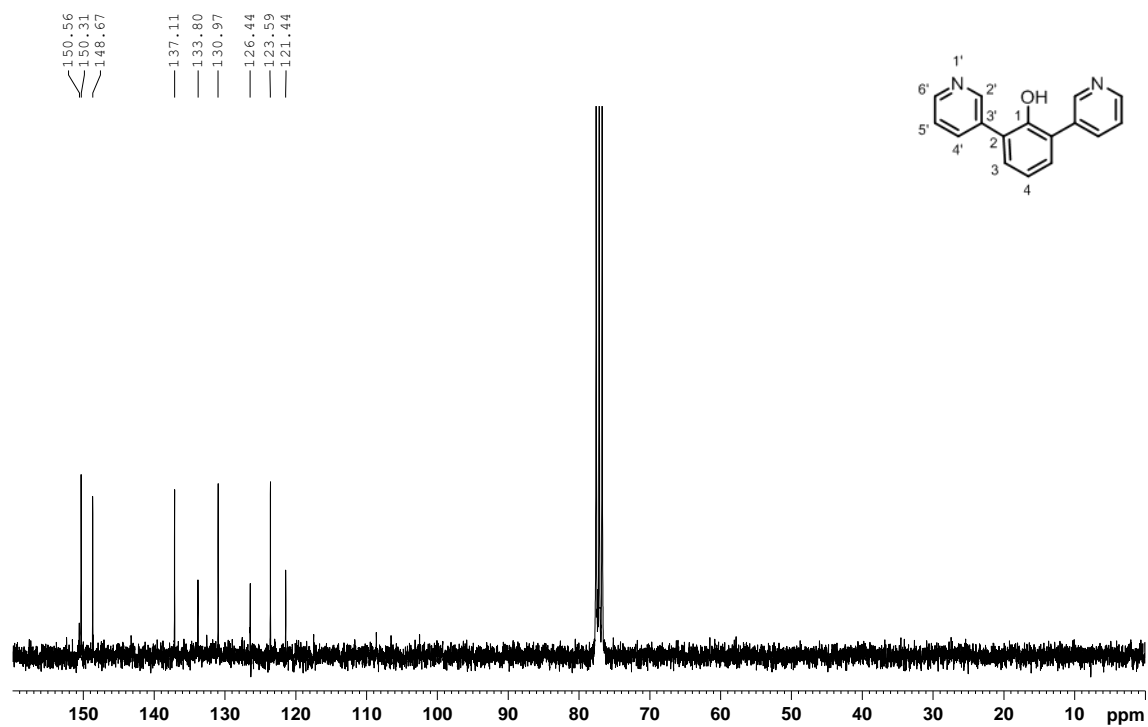
$^1\text{H-NMR}$ ,  $\text{CDCl}_3$ , 300 MHz



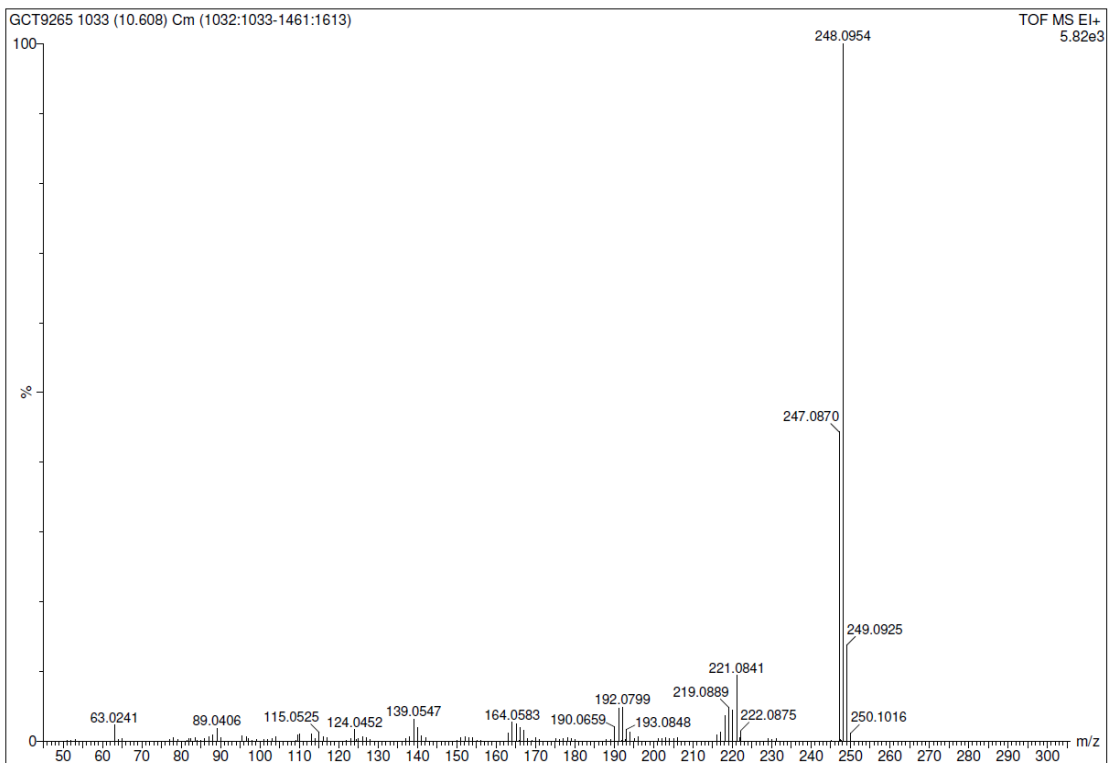
*COSY NMR*



$^{13}\text{C-NMR}$ ,  $\text{CDCl}_3$ , 74 MHz

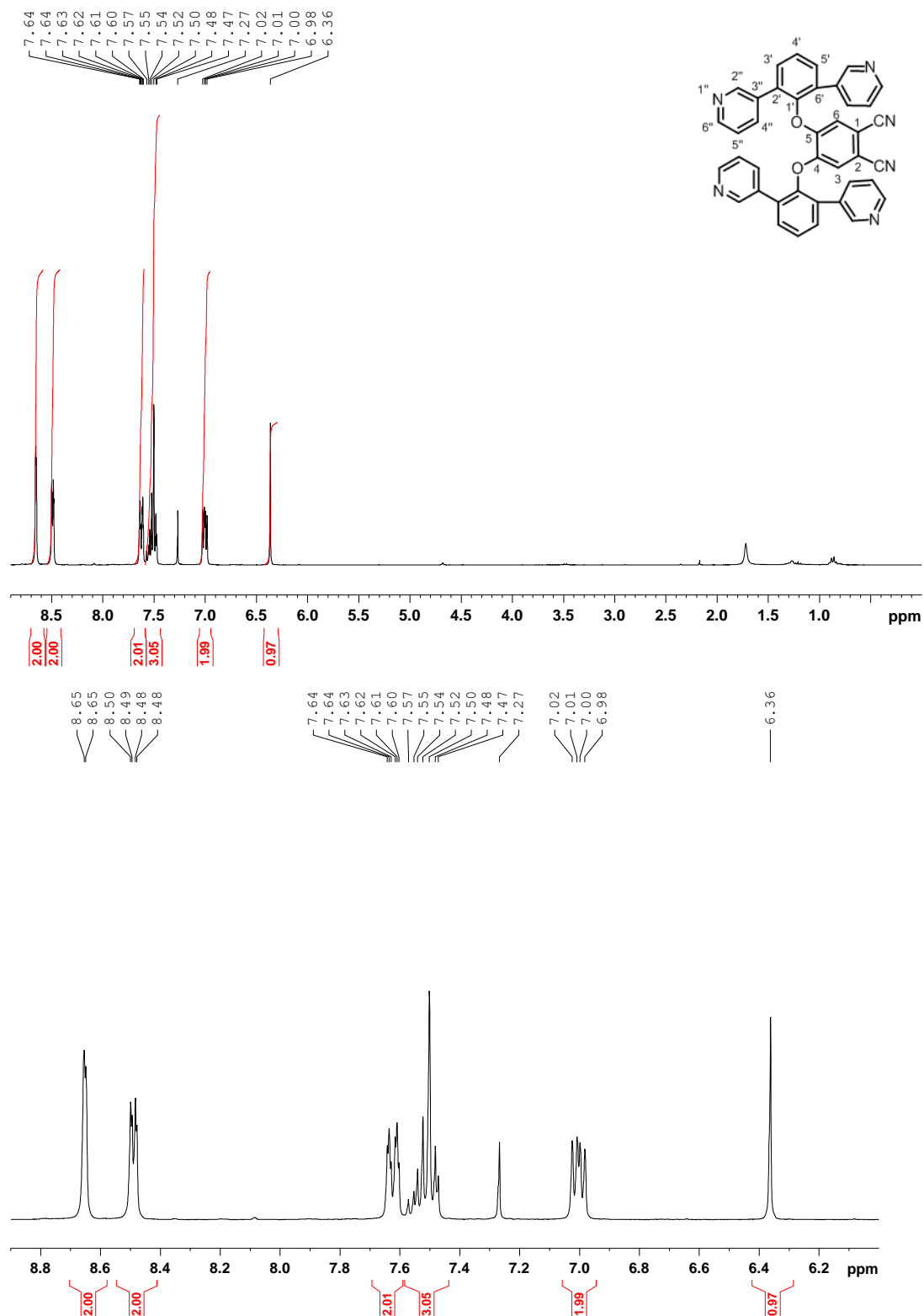


*ESI mass spectrum*

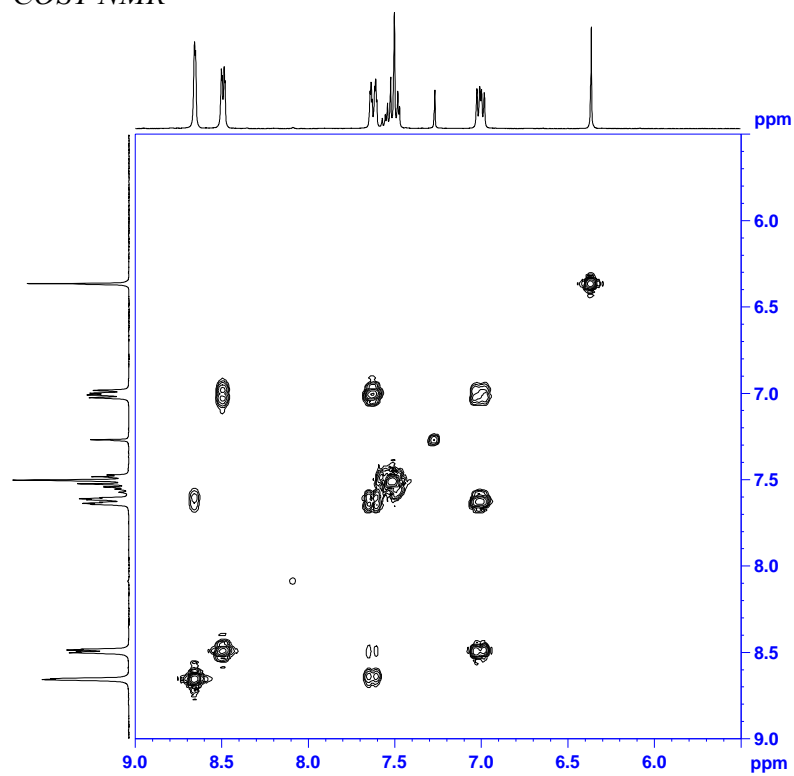


4,5-bis(-2,6-di(pyridin-3-yl)phenyl)phthalonitrile (7)

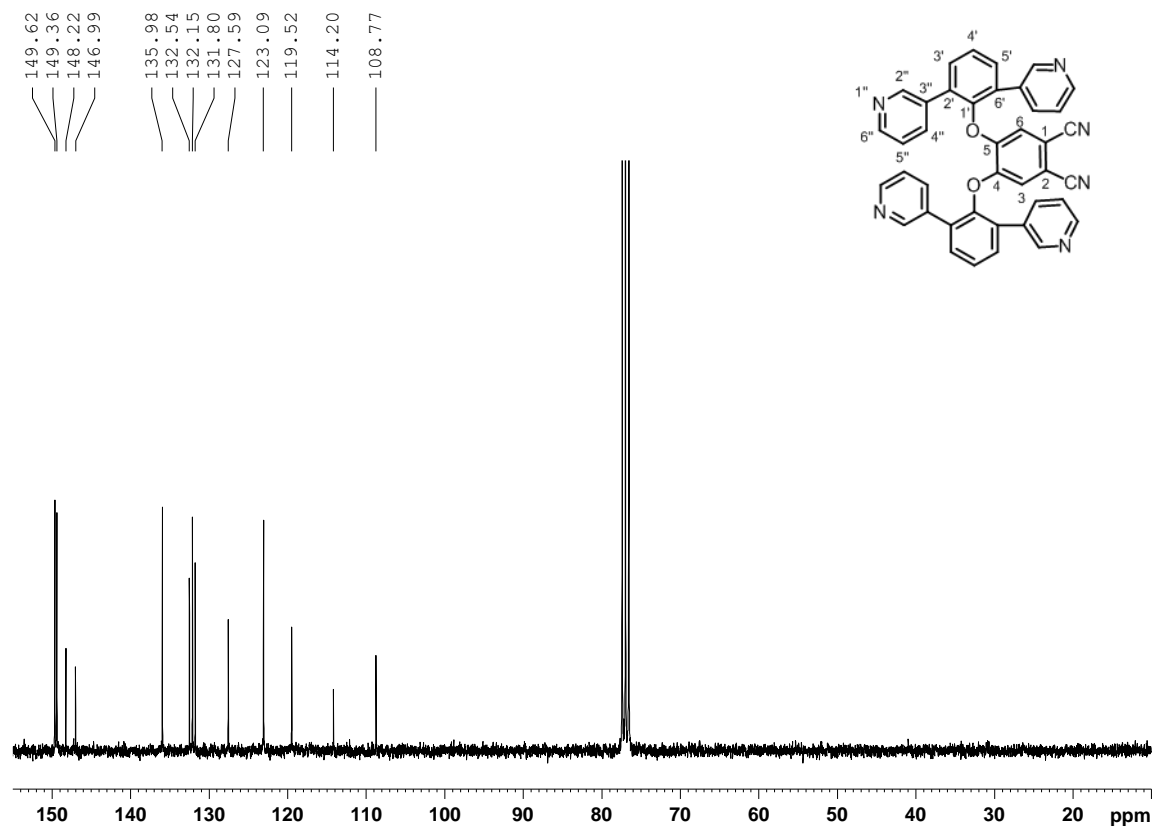
$^1\text{H-NMR}$ ,  $\text{CDCl}_3$ , 300 MHz

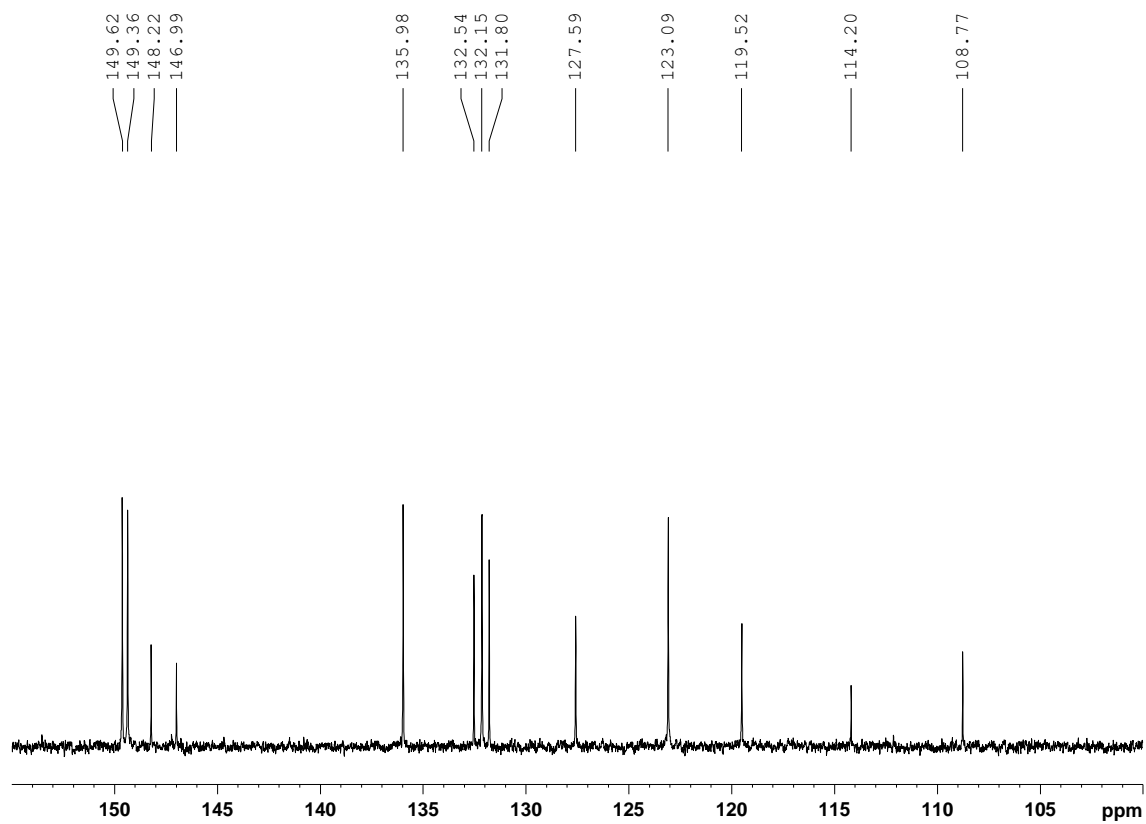


COSY NMR

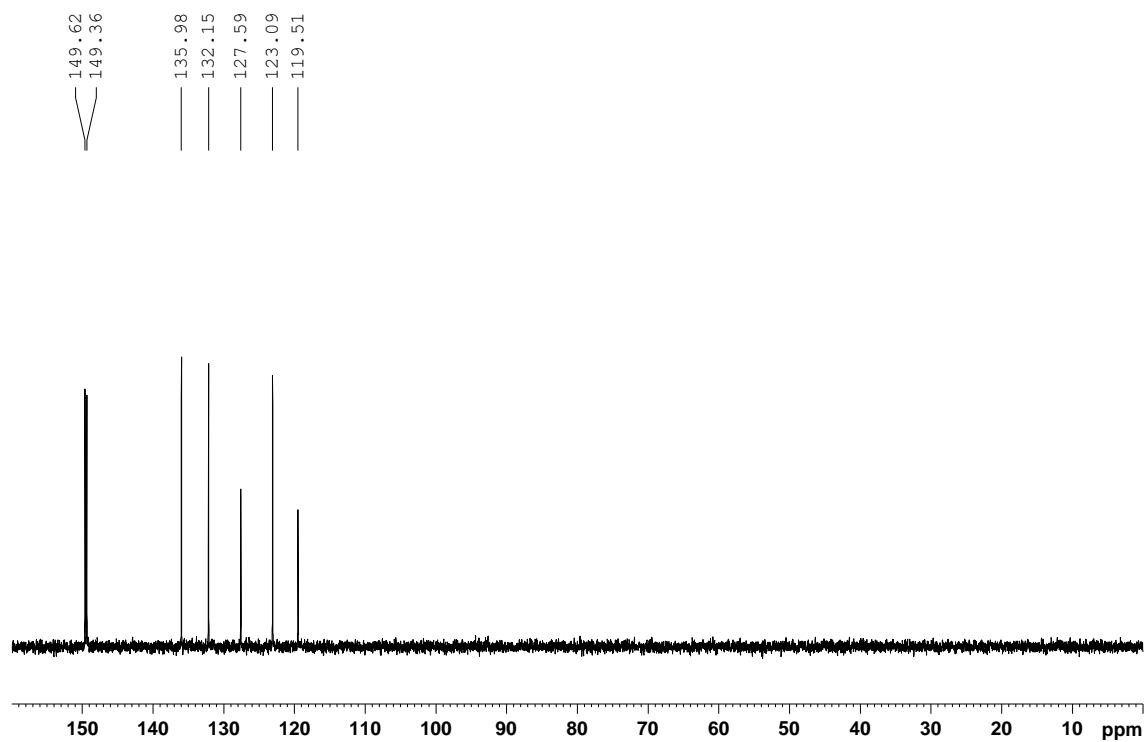


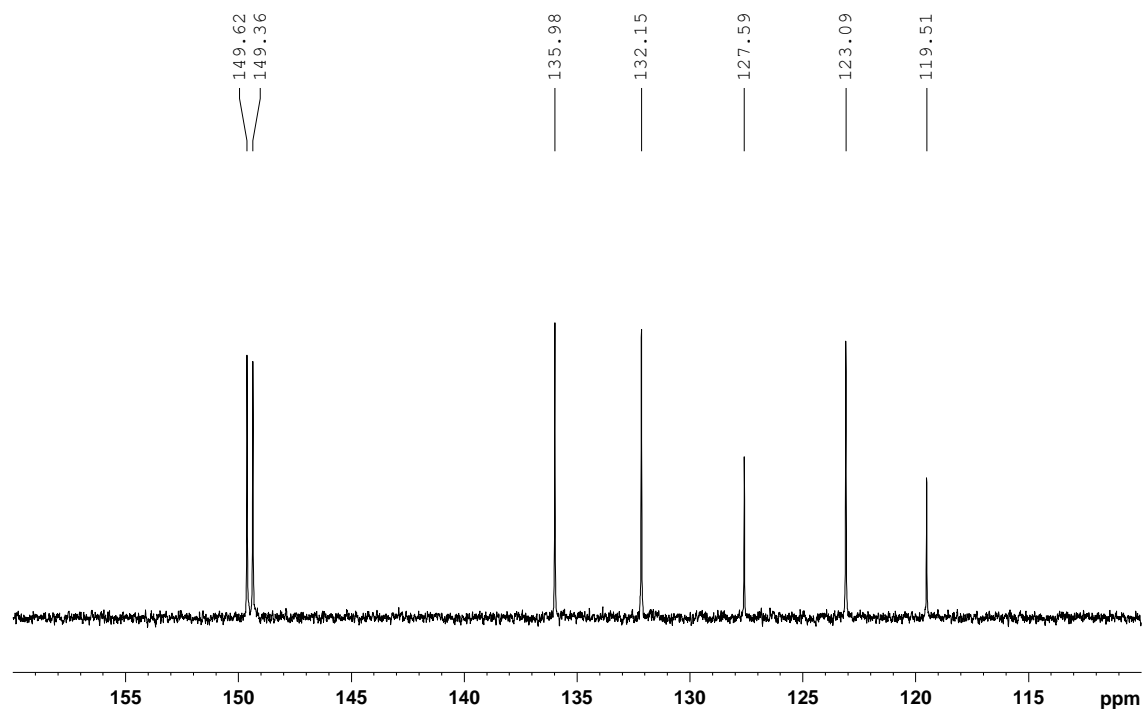
$^{13}\text{C}$ -NMR,  $\text{CDCl}_3$ , 74 MHz



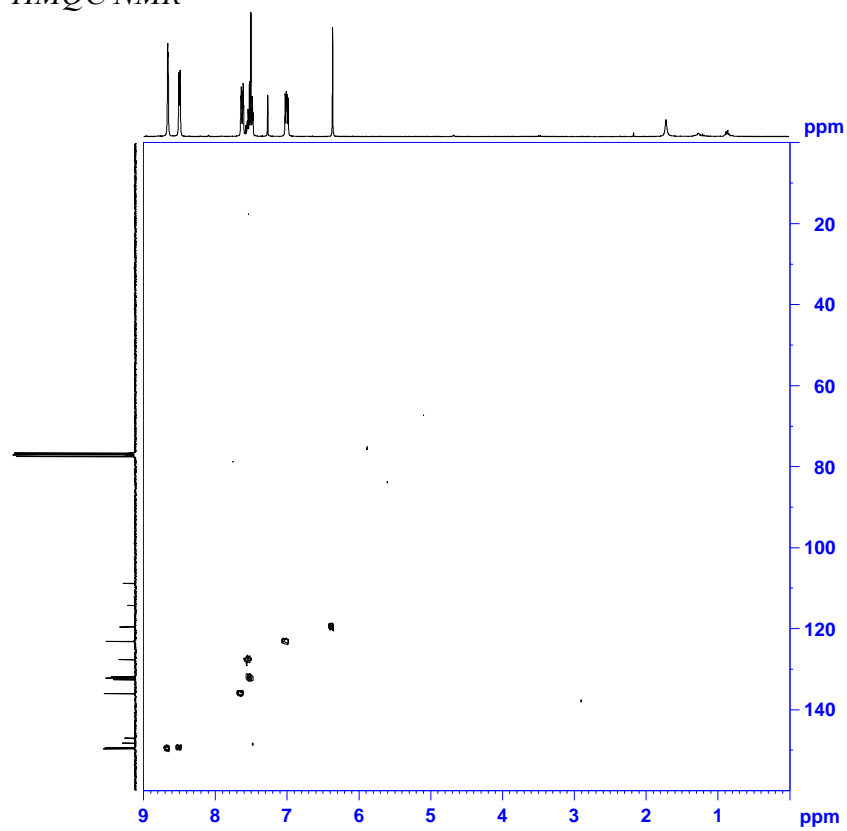


### *135-DEPT NMR*

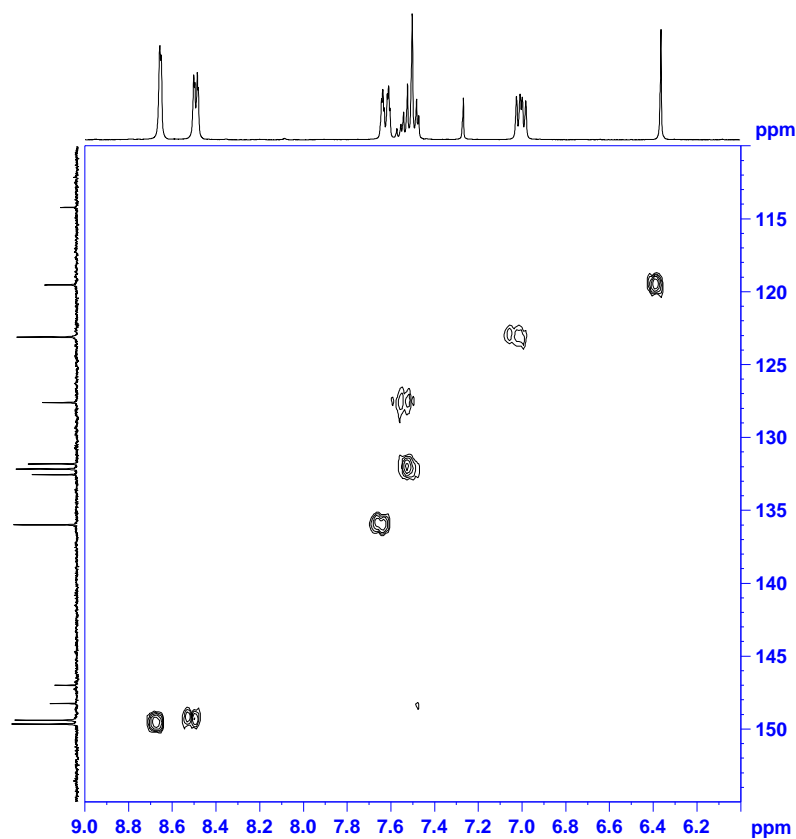




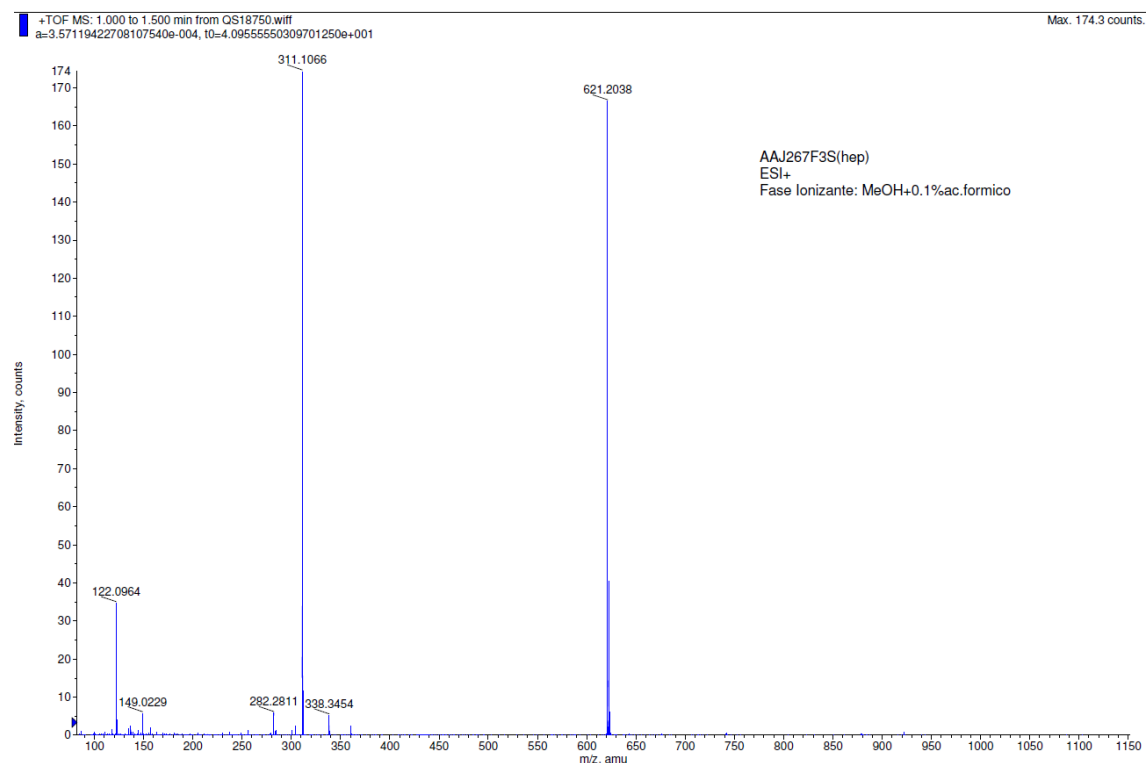
*HMQC NMR*





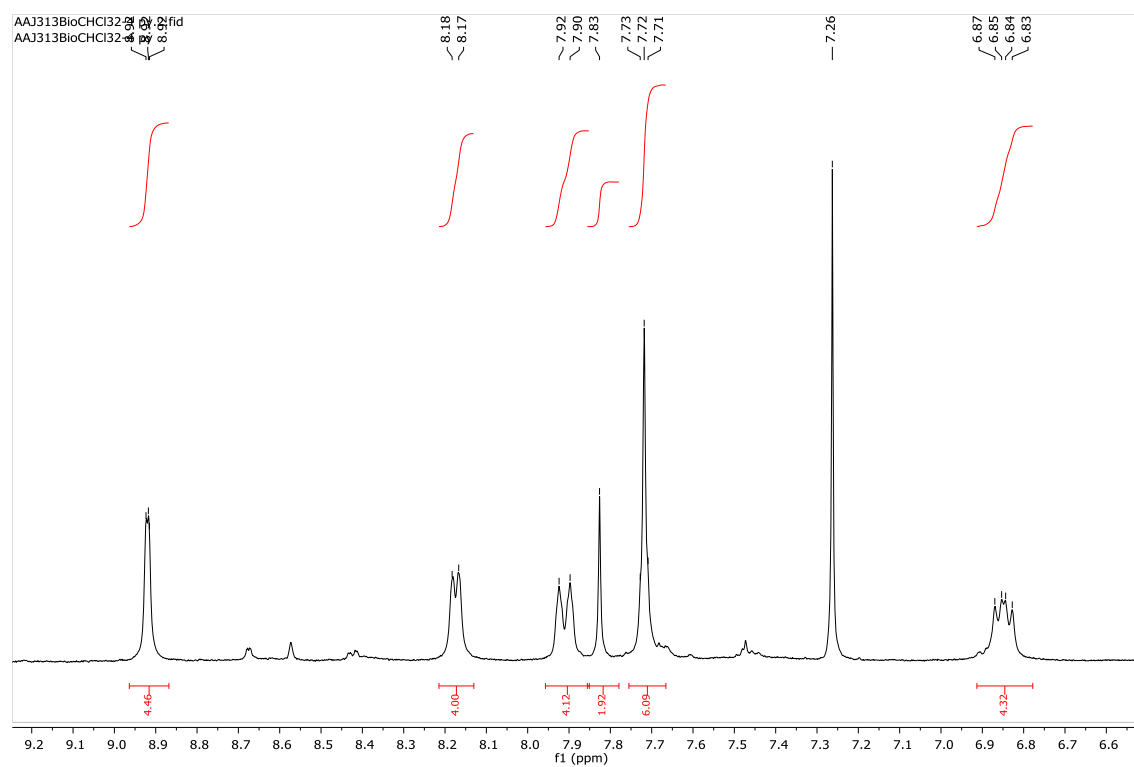
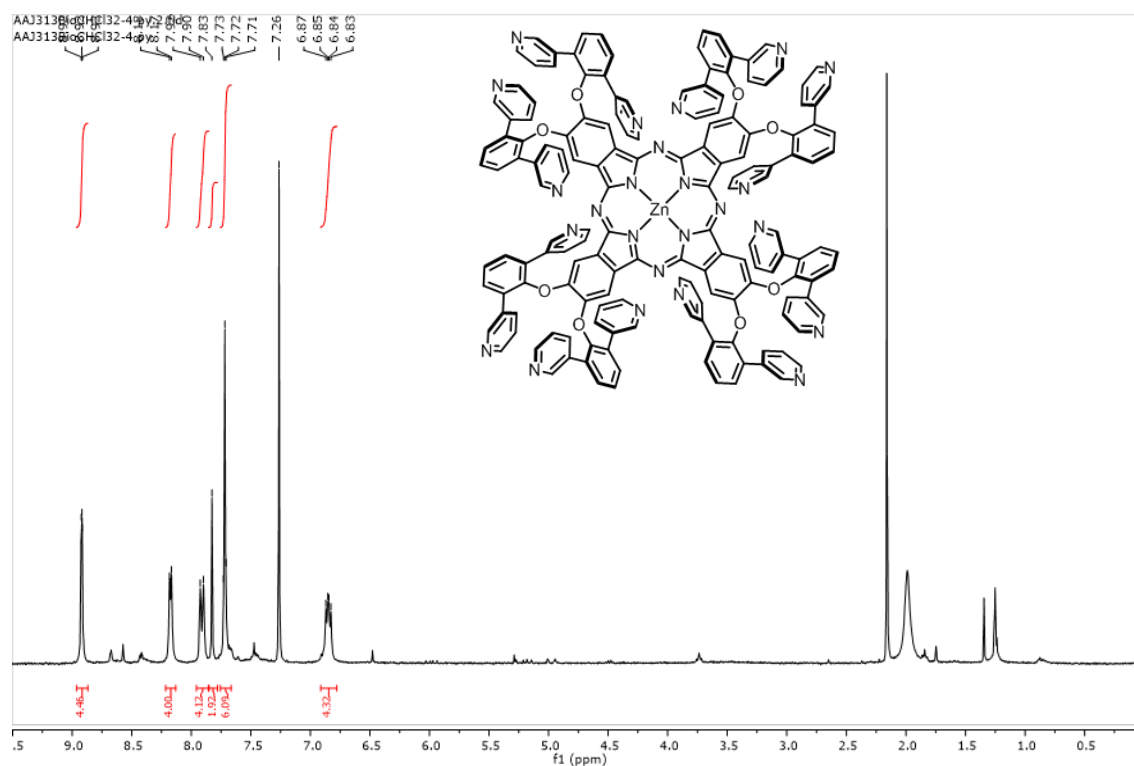


### ESI mass spectrum

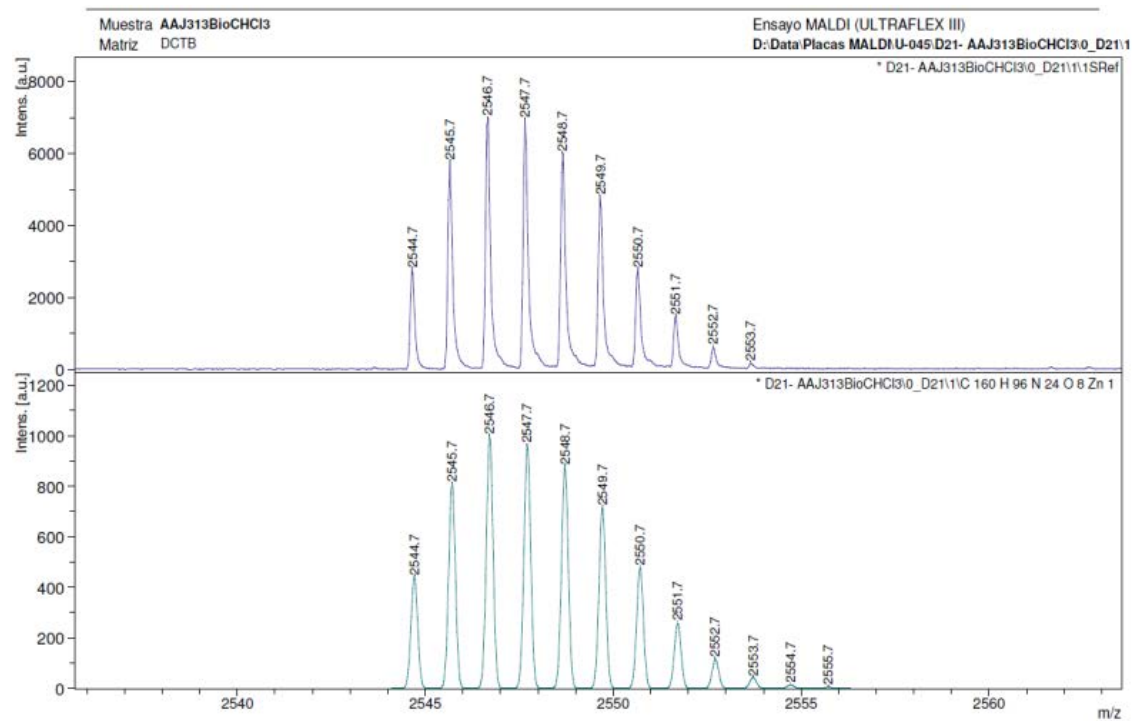
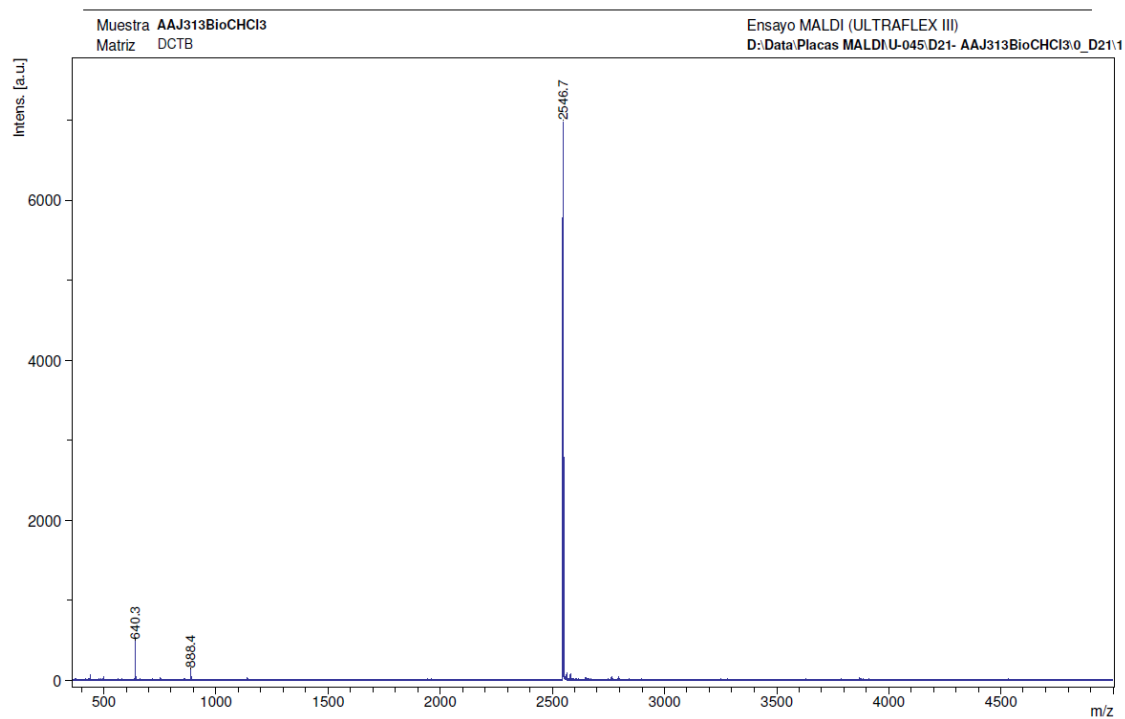


## Zinc(II)phtalocyanine (**8**)

$^1\text{H-NMR}$ ,  $\text{CDCl}_3$ , 300 MHz

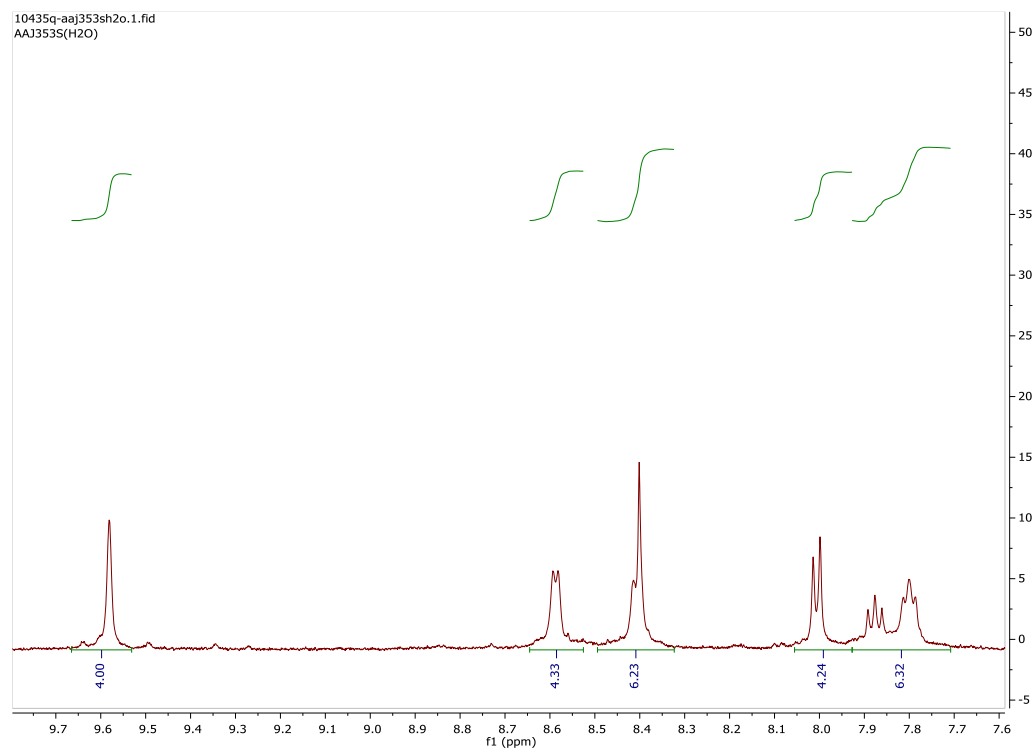
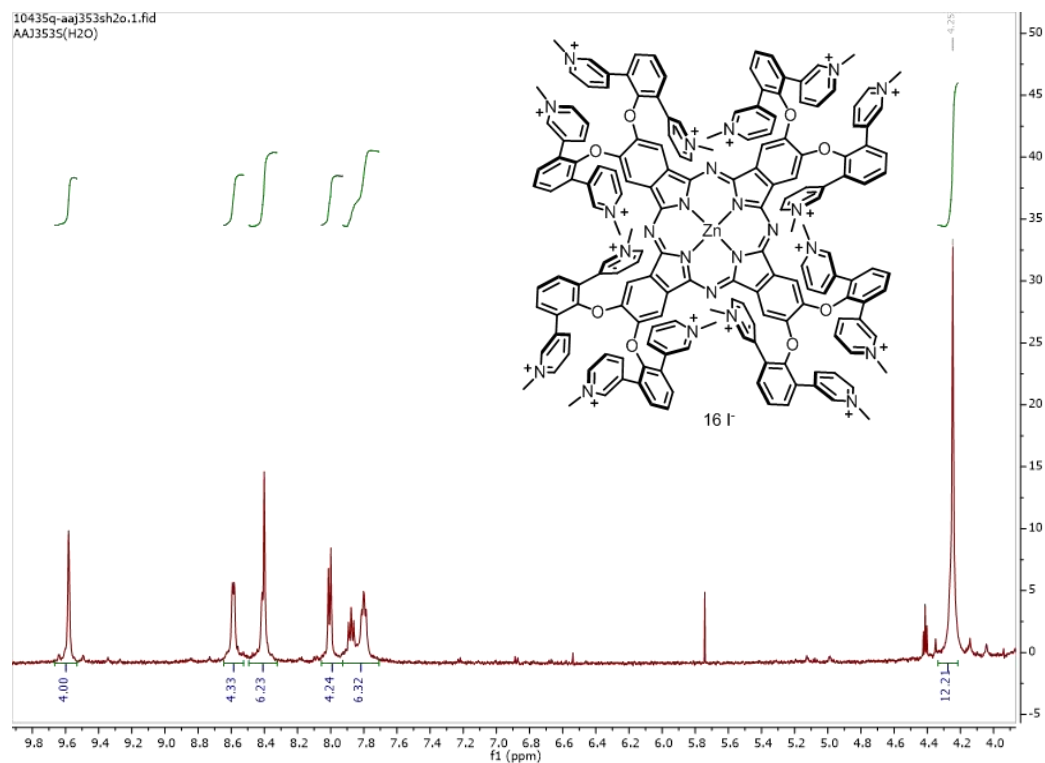


## MALDI mass spectrum

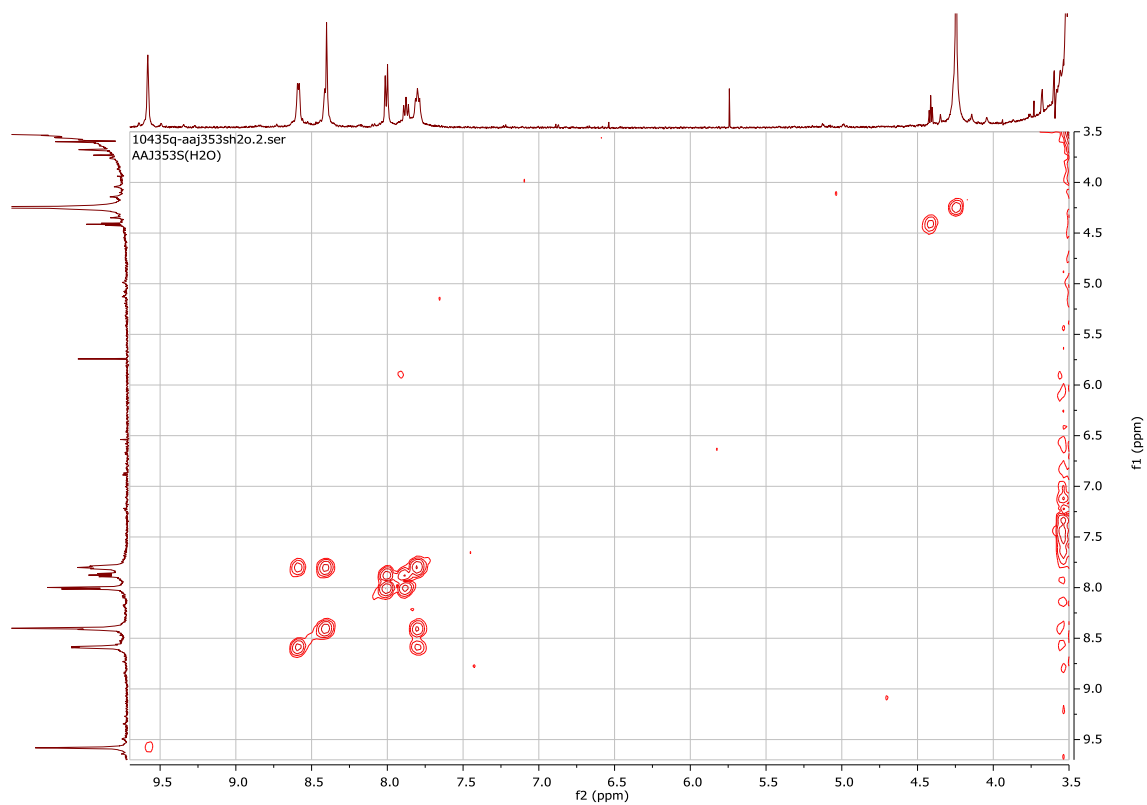


## Hexadecacationic Zn(II)phthalocyanine (**1**)

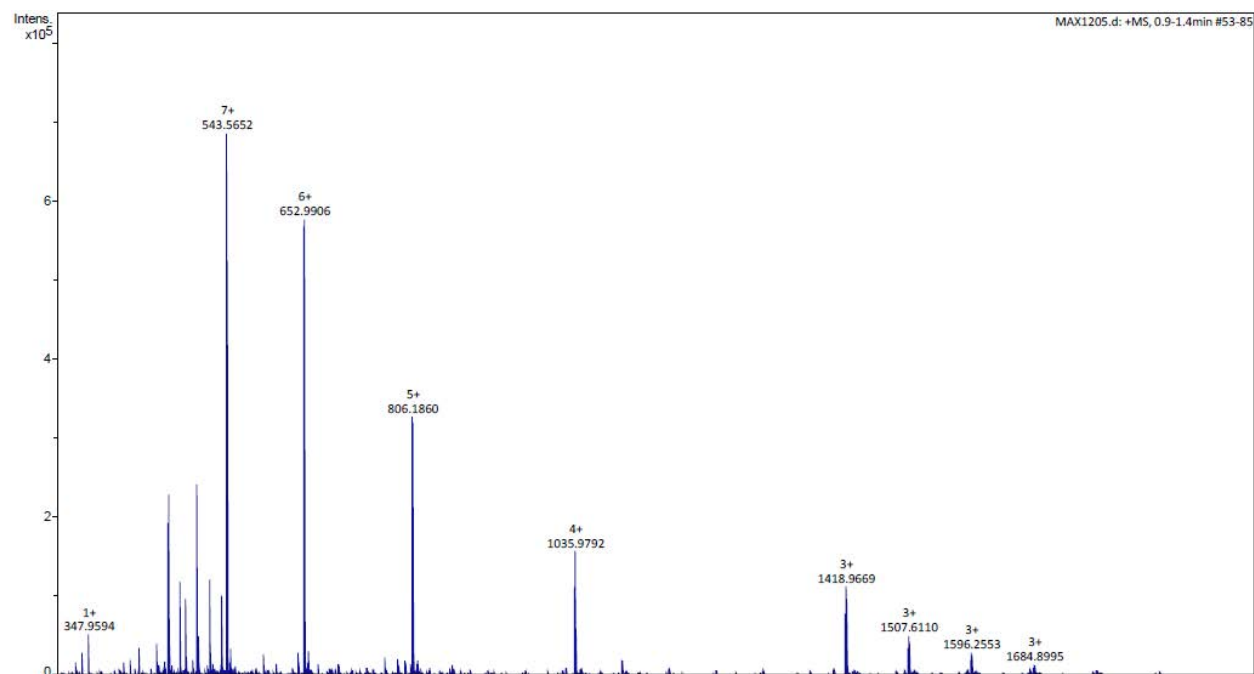
$^1\text{H-NMR}$ ,  $\text{CDCl}_3$ , 300 MHz

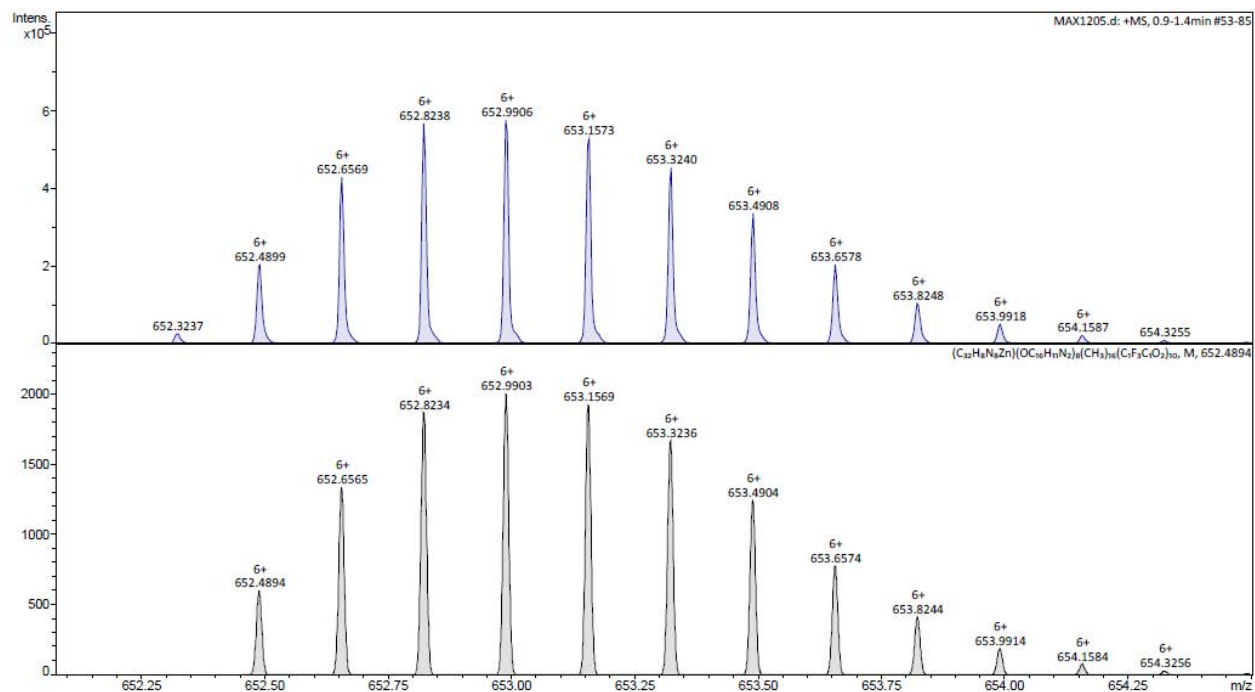
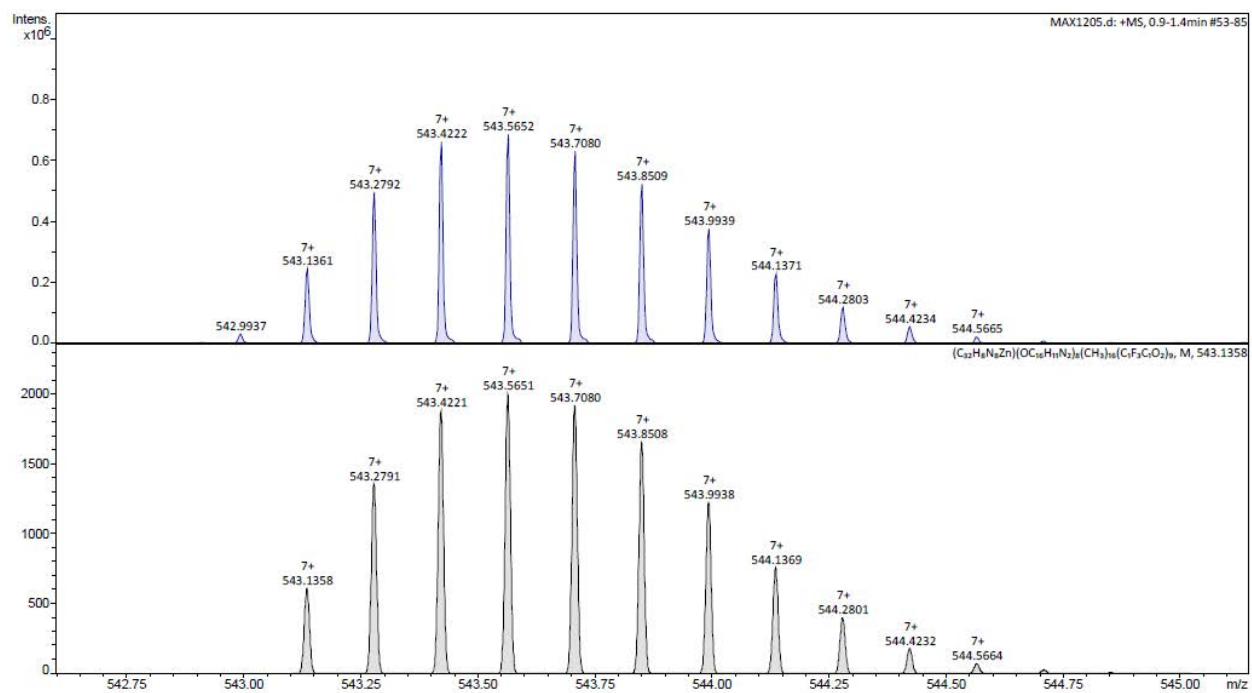


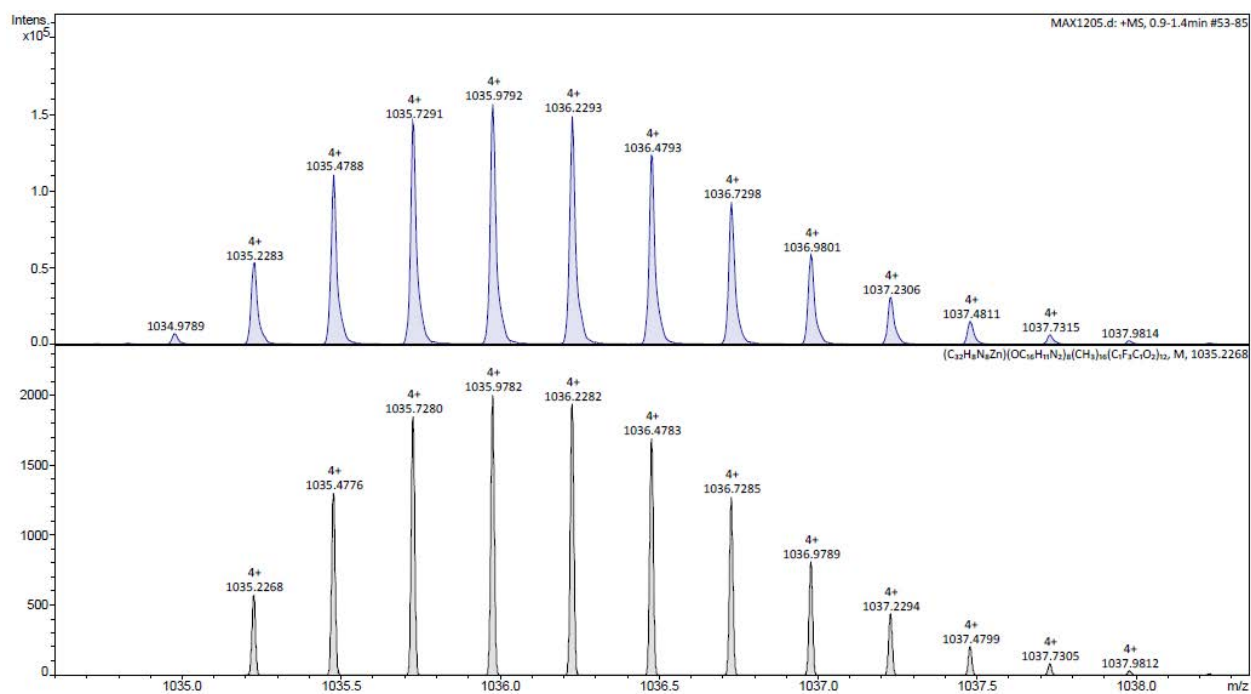
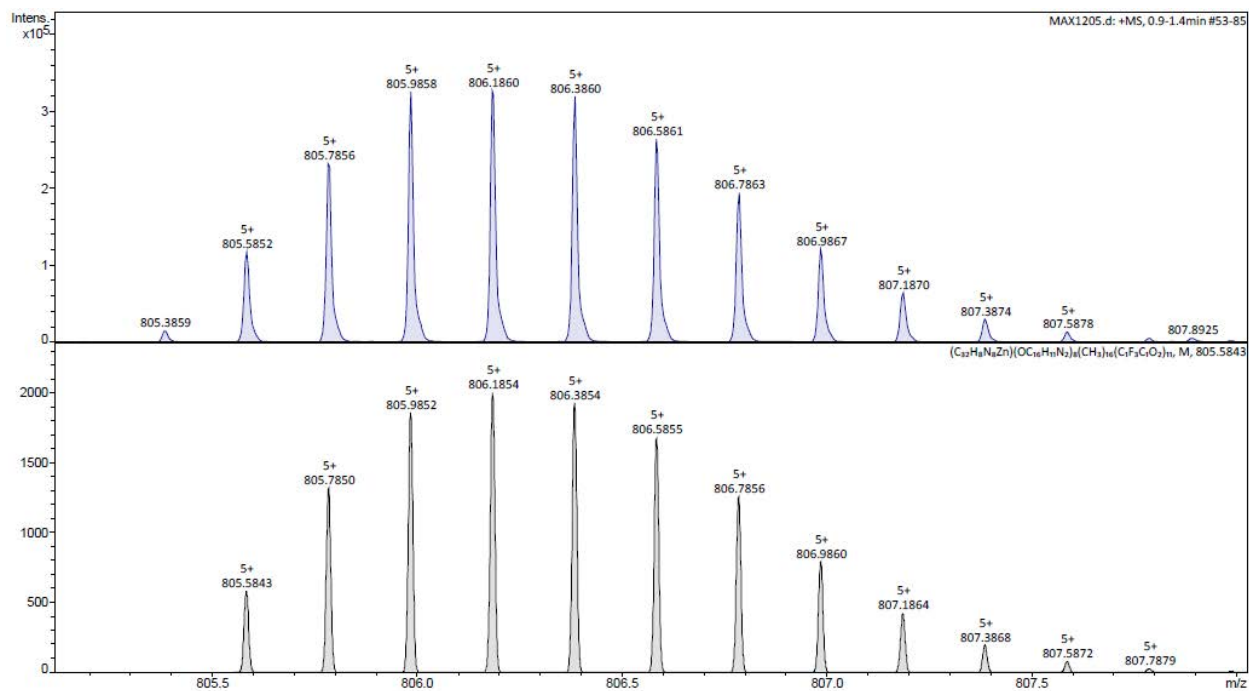
COSY NMR

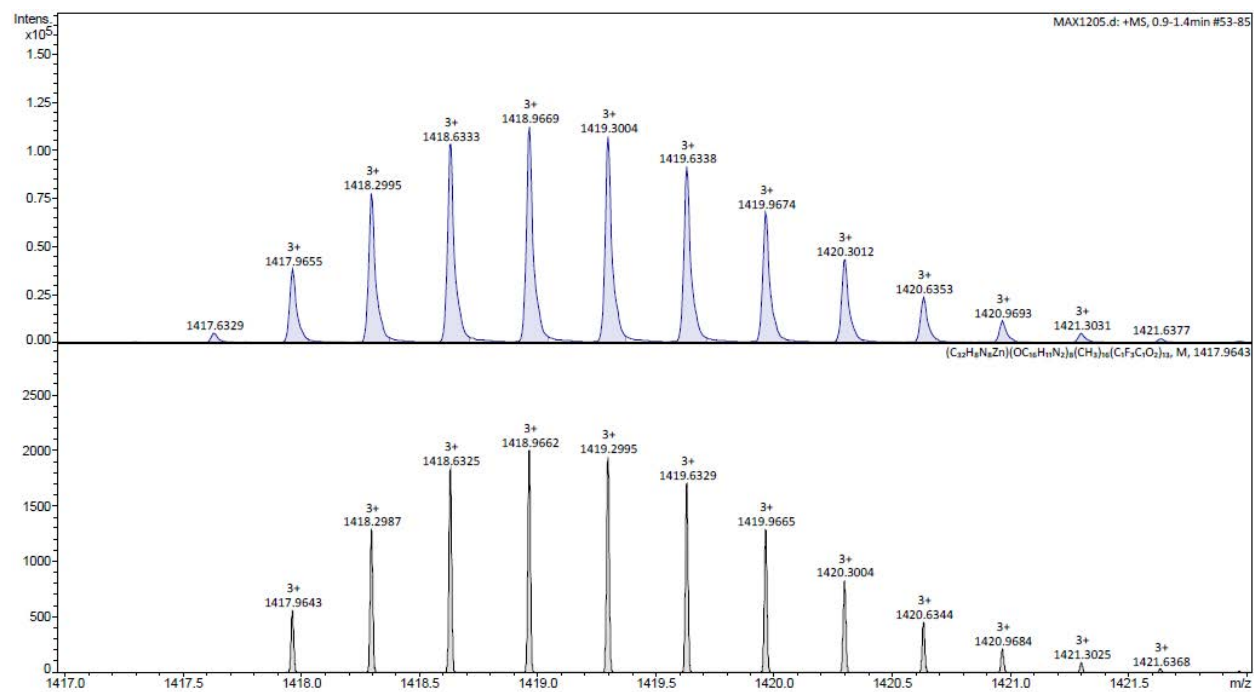
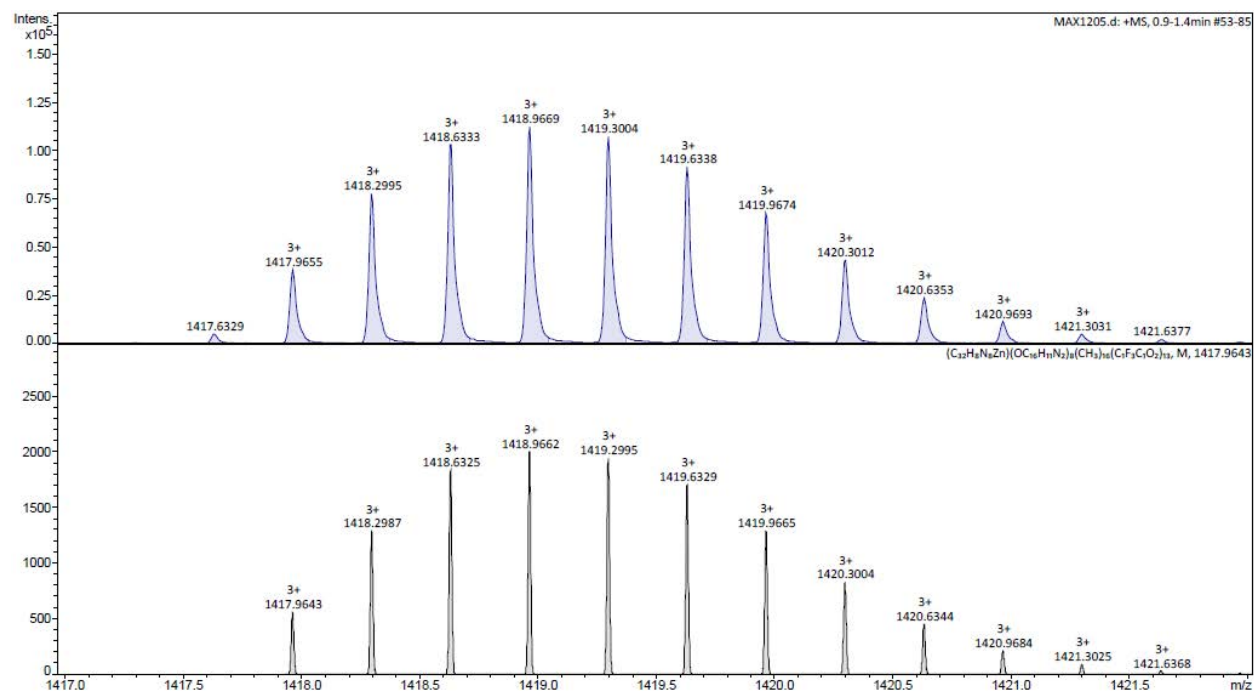


### ESI mass spectrum











## 11. Bibliography

- [1] D. Mastronarde, *Microsc. Microanal.* **2003**, 9, 1182.
- [2] J. R. Kremer, D. N. Mastronarde, J. R. McIntosh, *J. Struct. Biol.* **1996**, 116, 71.
- [3] P. Engelhardt, Three-Dimensional Reconstruction of Chromosomes Using Electron Tomography. in *Electron Microscopy: Methods and Protocols* (ed. Kuo, J.) pp 365 (Humana Press, 2007).
- [4] P. Engelhardt, *Encycl. Anal. Chem.* **2000**, 4948.
- [5] V. Liljeström, A. Ora, J. Hassinen, H. T. Rekola, N. Nonappa, M. Heilala, V. Hynninen, J. Joensuu, R. H. A. Ras, P. Törmä, O. Ikkala, M. A. Kostainen, *Nat. Commun.* **2017**, 8, 671.
- [6] H. Li, T. J. Jensen, F. R. Fronczek, M. G. H. Vicente, *J. Med. Chem.* **2008**, 51, 502.
- [7] J. Zhao, M. Riediker, *J. Nanoparticle Res.* **2014**, 16, 2493.
- [8] W. Li, D. P. Nelson, M. S. Jensen, R. S. Hoerrner, D. Cai, R. D. Larsen, P. J. Reider, *J. Org. Chem.* **2002**, 67, 5394.
- [9] A. Nedoluzhko, T. Douglas, *Journal of Inorganic Biochemistry* **2001**, 84, 233.